Biophysics of sodium channels during subthreshold depolarization *in vitro* and *in silico*

Phil Alexander Köster[a], Thomas Stiehl[b,c], Jenny Tigerholm[c], Anna Maxion[a,d], Barbara Namer[a,d], Angelika Lampert[a*]

[a]University Hospital, RWTH Aachen University, Institute for Neurophysiology, Pauwelsstrasse 30, 52074 Aachen, Germany

[b]University Hospital, RWTH Aachen University, Institute for Computational Biomedicine and Disease modelling with focus on phase transitions between phenotypes, Pauwelsstrasse 30, 52074 Aachen, Germany

[c]University Hospital, RWTH Aachen University, Joint Research Center for Computational Biomedicine (JRCC), Pauwelsstrasse 30, 52074 Aachen, Germany

[d]University Hospital, RWTH Aachen University, Interdisciplinary Center for Clinical Research (IZKF), Faculty of Medicine, Research Group Neurosciences, Pauwelsstrasse 30, 52074 Aachen, Germany

[*]Corresponding author:
Angelika Lampert
Institute for Neurophysiology, University Hospital, RWTH Aachen University
Pauwelsstrasse 30
52074 Aachen, Germany
E-mail: alampert@ukaachen.de
ORCID: https://orcid.org/0000-0001-6319-6272

Abstract

Voltage-gated sodium channels (VGSC) are responsible for the fast upstroke of an action potential (AP). In the peripheral nervous system, e.g., in sensory neurons responsible for detection of potentially painful stimuli, subthreshold depolarizations support the initiation of an AP. Nav1.7 was suggested to be a subthreshold channel, and recent studies from human cells assign it a role as threshold channel.

We examine the biophysical properties of heterologously expressed sensory neuron VGSCs Nav1.1-Nav1.5 and Nav1.6-Nav1.8 with focus on the subthreshold depolarization phase of APs in manual patch clamp. VGSCs were similar in their biophysical properties; except for Nav1.8 which gated at more depolarized and Nav1.5 at more hyperpolarized potentials. For Nav1.1, Nav1.2 and Nav1.8, but not the remaining tested VGSCs, a positive correlation between ramp current and window currents was detected. During AP clamp Nav1.7 and Nav1.3 generated currents with the largest area under the curve compared to the other channels tested here.

Experimental results were fitted by a modified Hodgkin-Huxley model and a simple AP was simulated. We adjusted the VGSC composition according to published RNAseq data to resemble a putative silent nociceptor and an Aδ-fiber. In both fiber types, the amount of Nav1.7 seems to strongly influence whether a neuron fires repetitively or not.

In summary, we provide a comprehensive, comparable set of patch-clamp data of most of the VGSCs relevant for nociception, which can be used as basis for computational modelling, disease modelling and the development of adapted, targeted future pain medication.

Introduction

The propagation of electrical stimuli through action potentials (AP) is a characteristic feature of excitable cells, such as cardiomyocytes or neurons of the central, visceral, or peripheral nervous system. Depending on the tissue type, different membrane ion channels contribute to the generation and propagation of APs. For the perception of pain, especially the family of voltage-gated sodium channels (VGSC) determines and regulates the cellular excitability (Bhattacharjee et al. 2018, Bennett et al. 2019, Goodwin and McMahon 2021).

Mammalian VGSC consist of α and β-subunits. To this date, nine mammalian VGSC α subunits (Nav1.1 – Nav1.9) have been described, encoded by the genes SCN1A-SCN5A and SCN8A-SCN11A which are sufficient for current conductance (Yu and Catterall 2003, Catterall et al. 2005, Dib-Hajj et al. 2010). Although all are fast gating ion channels (within milliseconds) VGSC α-subunits differ in their biophysical properties, e.g., activation, inactivation and deactivation occur at different speed and membrane potentials (Ahern et al. 2016, Körner and Lampert 2020). They are categorized by their sensitivity toward tetrodotoxin (TTX), a neurotoxin from the pufferfish, with Nav1.5, Nav1.8, and Nav1.9 being resistant to TTX (TTXr), while the remaining channel isoforms are TTX-sensitive (TTXs) (de Lera Ruiz and Kraus 2015).

Excitable cells within the human body are characterized by distinct expression patterns of VGSCs, which in turn play a major part in the electrophysiological behaviour of that cell type (Catterall et al. 2005, Ahern et al. 2016). Nav1.1-Nav1.3 and Nav1.6 are predominantly expressed in central nervous system (CNS) neurons (Whitaker et al. 2000, Vacher et al. 2008, Liang et al. 2021), while Nav1.7-Nav1.9 primarily convey sensory information along peripheral nervous system (PNS) neurons such as dorsal root ganglion (DRG) neurons, sympathetic ganglion neurons or olfactory sensory neurons (Fukuoka et al. 2008, Wang et al. 2017). Nav1.4 and Nav1.5 channels are mainly expressed in skeletal and cardiac muscle cells, respectively (Sheets and Hanck 1999), although Nav1.5 can also be found in PNS neurons during development and injury (Renganathan et al. 2002).

Contribution of each VGSC isoform to the AP electrogenesis is still a subject of ongoing discussions. Nav1.8 is regarded as the main contributor to the upstroke and width of the AP (Renganathan et al. 2001, Blair and Bean 2002, Matsutomi et al. 2006, Han et al. 2015), while Nav1.9, eliciting large persistent currents, is thought to modify the resting membrane potential (RMP) and thereby enhancing subthreshold depolarization (Herzog et al. 2001, Maingret et al. 2008). The subthreshold depolarization of an AP is described to be supported by TTXs currents

(Enomoto et al. 2006, Vasylyev and Waxman 2012), but the specific contribution of each channel isoforms is yet to be understood.

VGSC expression patterns are neither disjunct nor unalterable: E.g., Nav1.3 expression was found to be present in embryonic, but not in adult rat DRG neurons, yet in adult mouse DRG neurons, Nav1.3 expression and currents were upregulated after spinal cord injury (Felts et al. 1997, Hains et al. 2003, Lampert et al. 2006). Recent spatial transcriptomics data from human DRG neurons reported fiber subtype specific mRNA expression of all VGSC isoforms (Tavares-Ferreira et al. 2022)

Nociceptive stimuli are conveyed by C- and Aδ-fibers. A specific C-fiber subclass, the so called "sleeping" or "silent" nociceptors, is prominently involved in the generation of neuropathic pain. In patients with ongoing pain, this fiber type shows spontaneous activity, which correlates with the patients' pain sensation (Kleggetveit et al. 2012). Somatosensory neurons for distinct subclasses which have their own distinct VGSC expression pattern, as revealed by RNAseq and bioinformatic analysis (Tavares-Ferreira et al. 2022).

Mutations in VGSC encoding genes can lead to several diseases, so called channelopathies, by altering the biophysical channel properties. Some mutations – mainly *gain-of-function* variants in Nav1.7 - are linked to inherited pain syndromes (Lampert et al. 2010, Bennett and Woods 2014, Brouwer et al. 2014, Dib-Hajj et al. 2017), such as erythromelalgia (Yang et al. 2004, Tang et al. 2015), paroxysmal extreme pain disorder (Fertleman et al. 2006, Jarecki et al. 2008), or small fiber neuropathy (Faber et al. 2012, Hoeijmakers et al. 2012, Huang et al. 2013). *Loss-of-function* mutations of Nav1.7 induce loss-of-pain syndromes such as congenital insensitivity to pain (Cox et al. 2006, Leipold et al. 2013, McDermott et al. 2019), suggesting that specifically the function and the amount of available Nav1.7 channel seems to be crucial for human sensation of potentially painful stimuli (nociception). Understanding of the underlying mechanisms could reveal targets for the development of new pain medication.

Nociceptive stimuli depolarize the cell membrane, but if they are small, they do not initiate an action potential. To this end several subthreshold depolarizations are needed to sum up, which are supported by VGSCs which open at potentials below threshold. For a long time, Nav1.7 was assumed to be the main channel depolarizing the cell membrane during the subthreshold phase as determined in heterologous expression systems (Rush et al. 2007, Vasylyev et al. 2014). Recently, however, in recordings of iPSC-derived human sensory neurons, its contribution to subthreshold depolarization was observed to be limited, and Nav1.7 was described as a threshold channel (Meents et al. (2019). The study found that a Nav1.7 *gain-of-*

function mutation causing inherited erythromelalgia (Nav1.7/I848T) reduced AP threshold but did not alter the subthreshold depolarization slope and argued that Nav1.7 might not be the main supporting force of the subthreshold phase, since it opens at more depolarized voltages than other TTXs channel isoforms.

In silico experiments are a resource-efficient way to generate and check hypotheses. They allow to systematically study complex systems by varying potentially influencing factors one by one in order to disentangle impacts on system behavior. Computational models provide insights into scenarios which are experimentally unfeasible or too costly and bear great potential for various fields of application, such as disease modelling or drug testing. In 1952, Hodgkin and Huxley provided a mathematical description of VGSC gating and APs, which still today is often used to model electrophysiological data (Hodgkin and Huxley 1952, Stiles and Gray 2021, Wang et al. 2022). Mostly, only a few VGSC subtypes are integrated in such models, also because of a lack of a comparable, comprehensive data sets which could be used for model generation. Larger studies which compare VGSC gating in the same experimental setting were focusing either on CNS VGSCs and their mutations leading e.g. to epilepsy (Thompson et al. 2023), or on sensory neuron sodium channels and their temperature dependence (Kriegeskorte et al. 2023).

As conclusive and complete data of the sub- and suprathreshold activity of all VGSC isoforms is not yet available, we here perform a standardized and comparative examination with consistent experimental conditions of VGSC isoforms involved in nociception. We performed patch-clamp experiments in heterologous expression systems (HEK293 and ND7/23 cells) to examine the sub- und suprathreshold gating during ramp stimulation, AP clamp and step depolarizations of each channel isoform individually (Meents and Lampert 2016, Rogers et al. 2016). Wild-type Nav1.9 is known to show poor heterologous expression and was therefore not part of this study. A Nav1.9 chimera with a fused Nav1.4 C-terminus (Goral et al. 2015) expresses better, but is known to alter biophysical properties (e.g., voltage shift in steady-state fast inactivation). Thus, we did not include Nav1.9 in this study.

Neuronal excitability of nociceptors has been modelled using e.g., a simulation of a C-fiber ending (Tigerholm et al. 2014). Here, we solely focus on the role of each VGSC subtype to AP generation. Thus, we created a computational model based on Hodgkin-Huxley, in which we implement the VGSC subtype contribution as reported for putative sleeping nociceptors and Aδ-fibers (Tavares-Ferreira et al. 2022) to investigate VGSC subtype contributions to excitability and AP generation.

Materials and Methods

Cell culture and cell preparation

Cell lines

Plasmids of VGSC isoforms considered in this study were either transfected stably in human embryonic kidney cell line HEK293 (rat Nav1.3 = rNav1.3, human Nav1.5 = hNav1.5, mouse Nav1.6 = mNav1.6, hNav1.7) or transiently in human embryonic kidney cell line HEK293T (hNav1.1, hNav1.2) or mouse/rat hybridoma nerve cell line ND7/23 (hNav1.8).

All used cell lines were cultivated adherently under standard cell culture conditions (i.e., 37°C and 5 % CO2) in their respective cell culture media and supplements (Table S1). Passaging for all cell lines was performed twice per week at approximately 80% confluency using Accutase (Sigma-Aldrich, St. Louis, Missouri, USA) with a 1:5 – 1:10 passaging rate onto cultureware coated with Geltrex (LDEV-Free, hESC-Qualified; Gibco, Thermo Fisher Scientific, Waltham, Massachusetts, USA). Only cells under the passage number of 30 were used for electrophysiological experiments.

Plasmids

Plasmid constructs used for transient transfection were amplified using XL10-gold ultracompetent cells (Agilent Technologies Inc., Santa Clara, California, USA) and verified by restriction pattern analysis and commercial DNA sequencing (Eurofins Genomics GmbH, Ebersberg, Germany). The plasmids for hNav1.1 (pCMV6-AC-hNav1.1 WT RRSSV 3' UTR, Myc-DDK) and hNav1.2 (pCMV6-XL5-hNav1.2 WT RRSSV 3' UTR) were kindly gifted by Frank Bosmans, Ghent University, Belgium. hNav1.1 contained the common natural variation A1067T (allele frequency for T: 0.728). The hNav1.8 plasmid (pIRES puro3-hNav1.8 WT) contained the V1073A (allele frequency for A: 0.58).

Transient transfection

HEK293T and ND7/23 cells were seeded in 35 mm² petri dishes 20-24 hours prior to transient transfection to reach a 70-90% confluency. Transfection was then performed using 3 µl jetPEI (Polyplus-transfection, Illkirch, France), 0.25 µg reporter plasmid pMax-GFP (Lonza, Basel, Switzerland) and 1.25 µg plasmid of the VGSC to be examined (N/P ratio ≈ 5). Cells were incubated for another 18-24 hours before being split onto fresh 35 mm² petri dishes. About 2 hours later, after the seeded cells attached to the cultureware, cells with a bright green fluorescence were used for patch clamp experiments.

Electrophysiology

General patch clamp framework

Electrophysiological experiments were performed as whole-cell voltage clamp using an EPC10-USB amplifier (HEKA Elektronik GmbH, Lambrecht/Pfalz, Germany). Cells were covered in extracellular solution (ECS), consisting out of 140 mM NaCl, 3 mM KCl, 1 mM $MgCl_2$, 1 mM $CaCl_2$, 10 mM HEPES and 20 mM Glucose. ECS was adjusted to pH 7.4 using NaOH, while osmolarity was between 305 and 312 mosm/l. Since ND7/23 cells display endogenous VGSC-mediated currents sensitive to tetrodotoxin (TTX) (Rogers et al. 2016, Lee et al. 2019), 500 nM TTX (Tocris, Bristol, United Kingdom) was added to the ECS for measurements of the TTX-resistant (TTXr) channel $hNa_v1.8$.

Glass pipettes from borosilicate glass fibers (Biomedical Instruments, Zöllnitz, Germany) were manufactured and fire-polished using a DMZ pipette puller (Zeitz Instruments GmbH, Martinsried, Germany). Pipette tip resistance (R_{pip}) was between 0,8 and 2 MΩ for all measurements. The pipette tip was filled with intracellular solution (ICS) containing 10 mM NaCl, 140 mM CsF, 1 mM EGTA, 10 mM HEPES and 18 mM Sucrose. ICS was adjusted to pH 7.31 with CsOH, while osmolarity was 313 mosm/l.

Experiments were conducted at room temperature (22 ± 1°C). Cells were kept in ECS for a maximum amount of 90 minutes, before being discarded. Cell size was between 5 and 33 pF. For all measurements, seal resistance (R_{seal}) was above 0,8 MΩ. At all times, series resistance (R_s) was below 5 MΩ and the voltage error (R_s * I) was below 5 mV. Only cells with a minimum peak current of 500 pA during the voltage dependence of activation protocol were considered.

Data was gathered using Patchmaster Next version 1.2 (HEKA Elektronik GmbH, Lambrecht/Pfalz, Germany). Analog signals were digitized at a sampling rate of 100 kHz (except for AP clamping measurements, which were sampled at 20 kHz) with a 10 kHz Bessel low-pass filter. Leak currents were measured and subtracted online (for activation, steady-state fast inactivation and ramp current measurements) or offline (for AP clamping due to technical limitations) with a *P/n* procedure (n = 4) preceding the respective test pulse. Capacitive currents were cancelled, and series resistance was compensated for by at least 75%. All measurements were corrected for a liquid junction potential (LJP) of 8.2 mV.

Patch clamp protocols

For each cell, stimulation protocols were only recorded once (no technical replicates). Protocols are indicated in the respective figures. For all protocols, the holding potential in between test pulses (V_{hold}) was set to -120 mV.

After establishing whole-cell configuration, a current stabilization protocol was conducted for 5 minutes, in which cells were held at holding potential and repeatedly stimulated with test pulses to 0 mV every 10 seconds.

To investigate the voltage dependence of activation, a series of 40 ms pulses from holding potential to a test pulse potential was elicited, with the test pulse potential increasing stepwise from -90 mV to +40 mV in 10 mV increments (-60 mV to +70 mV for most Nav1.8 measurements). The interpulse interval was 5 s. For assessment of the voltage dependence of activation (i.e., the fraction of channels activated to an open state depending on the membrane potential), we calculated the voltage dependent sodium conductance (G_{Na}) for each test pulse, using the equation

$$G_{Na} = \frac{I_{Na}}{V_m - E_{rev}}$$

(Eq. 1)

with I_{Na} being the peak inward current at the respective test pulse voltage V_m, and E_{rev} being the sodium reversal potential individually determined for each cell. To exclude effects of varying cell size and current density G_{Na} values were normalized to the maximum conductance $G_{Na,\,max}$ of that cell, before being plotted against test pulse voltages.

During the voltage dependence of steady-state fast inactivation (SSFI) protocol, after being held at holding potential, cells were initially stimulated with a 500 ms prepulse, before being exposed to a 40 ms test pulse at 0 mV. From sweep to sweep, the prepulse voltage increased stepwise from -140 mV to -30 mV with 10 mV increments (-110 mV to 0 mV for most Nav1.8 measurements). Interpulse interval was 10 s. For investigation of the voltage dependency of steady-state fast inactivation (i.e., the transient currents elicited by all available non-inactivated channels), the peak inward current for each test pulse (I_{Na}) was normalized to the maximum inward current during inactivation measurement ($I_{Na,max}$) to exclude effects of varying cell size and current density. Normalized current values were plotted against the respective prepulse potential.

Voltage dependence of activation conductance-voltage curves and voltage dependence of steady-state inactivation current-voltage curves were fitted with non-linear regression within GraphPad Prism using the Boltzmann equation

$$\frac{G_{Na}}{G_{Na,max}} \; or \; \frac{I_{Na}}{I_{Na,max}} = bottom + \frac{top - bottom}{1 + e^{\frac{V_{50} - V_m}{k}}}$$

(Eq. 2)

with V_{50} being the membrane potential at half-maximal channel (in)activation in mV, V_m being the membrane voltage in mV and k being the slope factor in 1/mV. The top value of the sigmoid curve was constrained to 1 for both activation and inactivation measurements. The bottom value was constrained to 0 for activation measurements but was not constrained for inactivation measurements to examine the fraction of channels remaining open after steady-state fast inactivation. The goodness of fit was $R^2 > 0,9$ for all Boltzmann fits.

We equated the window current for each cell as the area under the curve (AUC) of the superimposed activation and steady-state fast inactivation Boltzmann fit curves. Because SSFI Boltzmann fits do not reach 0 values when approaching infinity voltages, the AUC was calculated with +60 mV as upper limit, since this was the highest voltage used for the activation protocol.

For ramp current measurements, cells were stimulated with depolarizing voltage ramps from holding potential to +20 mV at different ramp rates, namely 0.1, 0.2, 0.4, 0.6, 1.2, 2, 4, and 6 mV/ms. For each ramp rate, the measured current response was averaged from three consecutive sweeps. The maximum inward current and the voltage at which it occurs was measured, as well as the area under the curve (AUC) of the current response. Because especially for Nav1.8, the ramp current bell curve didn't return to 0 pA at the end of the ramp, the AUC was calculated only up to the maximum inward current.

To measure the VGSC current response to APs, three different pre-recorded APs (AP1 – AP3) measured in nociceptors derived from induced pluripotent stem cells (iPS) were used as a voltage command. The AP commands differ in their characteristics (Table 1), e.g., subthreshold voltage slope is between 0.2 and 2 mV/ms. The respective AP current response was averaged out of three consecutive sweeps. For each AP, we calculated the maximum inward current and AUC of both the total AP and of the subthreshold phase of the AP. For the latter, the slope of the elicited current was calculated as well.

	AP1	***AP2***	***AP3***
average resting membrane potential (mV)	-76,5219	-71,9109	-67,3578
AP threshold voltage (mV)	-60,1176	-61,1503	-40,9651
maximum AP voltage (mV)	9,98309	11,1723	59,3039
voltage amplitude of AP (mV)	86,5047	83,0826	126,662
minimum voltage of afterhyperpolarization (mV)	-71,6341	-67,7223	-59,742
AP half width (ms)	3,62766	2,38951	3,78085
time to AP peak (ms)	99,6	14,55	18
subthreshold slope (mV/ms)	0,208367	1,39313	1,84487
upstroke slope (mV/ms)	3,30663	10,6357	27,0997

Table 1: Properties of the pre-recorded action potentials used as voltage commands. Data was gathered from current clamp measurements of IPS-derived nociceptors using the Igor Pro software.

Current responses for ramp and AP clamping were normalized to the maximum inward current during activation measurement ($I_{Na,max}$) to exclude effects of varying cell size and current density.

Sample sizes and data exclusion

We performed an a-priori analysis to estimate the number of cells needed for each experiment. In a small pre-study with Nav1.3 and Nav1.7, the voltage at which the maximum inward ramp current appeared was compared, assuming normal distribution. Using the software G*Power version 3.1.9.7 (Heinrich-Heine-Universität, Düsseldorf, Germany) we calculated the sample size for each VGSC to be n = 27 (hedge's g* = 1.23 as a measure of the effect size d, two-tailed $\alpha = 0.05$ and power $(1-\beta) = 0.95$).

We designed the study to have groups of equal size. Group size variation might occur due to cells being excluded from analysis a-posteriori, e.g., because of measurement artifacts impeding data analysis. Also, as ramp current measurements frequently showed substantial drift, hampering with calculation of the AUC, the following exclusion criteria were set up for ramp current AUC measurements: cells with a drift larger than +100 pA or -500 pA as well as cells with a drift larger than 10% of the maximum inward current of its respective voltage dependence of activation measurement were excluded from analysis. We performed no outlier analysis or elimination.

Data analysis

Data analysis for electrophysiological experiments was blinded except for Nav1.5. Data gathered by electrophysiological experiments was analysed using FitMaster version 2x90.5 (HEKA Electronik GmbH, Lambrecht, Germany) and IgorPro version 6.37 (WaveMetrics Inc., Portland, Oregon, USA). IgorPro analysis procedures are available upon reasonable request. GraphPad Prism version 9.5.1 (GraphPad Software, San Diego, California, USA) was used for Boltzmann fits and statistical testing. Graphing of data was perfomed with IgorPro, GraphPad Prism and CorelDRAW 2017 version 19.0.0.328 (Alludo, Ottawa, Ontario, Canada).

Statistics

Data is presented as mean ± standard deviation (SD) unless stated otherwise. Error bars denote the SD, while box plot whiskers show the 10th and 90th percentile. Threshold for statistical

significance was set to $p < 0.05$. P values are shown with 4 decimal places and summarized as follows: ns = $p > 0.05$, * = $p < 0.05$, ** = $p < 0.01$, *** = $p < 0.001$, **** = $p < 0.0001$.

Data was tested for normal distribution using the D'Agostino & Pearson omnibus K2 test. Normal distribution for an experiment was only assumed if each group passed the test individually. For statistical testing, groups were compared by ordinary one-way ANOVA with Tukey-Kramer's multiple comparisons test and a single pooled variance for parametric testing or Kruskal-Wallis test with Dunn's multiple comparison test for non-parametric testing. Values derived from ramp current measurements (I_{max}, $U_{location\ of\ Imax}$ and AUC) were compared by ordinary two-way ANOVA with Tukey-Kramer's multiple comparisons test and individual variances computed for each comparison, to compare between both VGSC isoforms and an additional factor of influence, i.e., the ramp rate. For correlations, we computed the nonparametric Spearman correlation with a two-tailed p value (data is given as Spearman's r with 95% CI) and graphed it with simple linear regression. Data was not matched nor paired.

The exact group n values are not shown in the figures for readability purposes but indicated in their respective tables and supplementary tables.

Computational modelling

To simulate the AP of a putative silent nocicepetor and an Aδ-fiber we use a modified version of the Hodgkin-Huxley model. Compared to the original Hodgkin-Huxley model (Hodgkin and Huxley 1952) we introduced a delay for current decay (fast inactivation kinetics). This modification prevents premature inactivation of sodium channels and improves the fit of the model to sodium currents for activation voltages above 10mV. The gating variables and the delay of inactivation were fitted using voltage clamp data for Nav1.1-Nav1.3 and Nav1.6-Nav1.8 acquired at room temperature (22 ± 1°C). The fits were performed with *fmincon* from the Matlab software R2021b (The MathWorks, Inc., Natick, Massachusetts, USA) using a multistart approach with latin hypercube sampling and a weighted least squares cost functional. To simulate APs in a putative silent nociceptor and an Aδ-fiber the ratios between the maximal conductances for considered VGSC subtypes were chosen to match recently published putative gene-expressions quantified in human DRG by spatial transcriptomics (Tavares-Ferreira et al. 2022). The simulations are based on the quantifications of gating variables at room temperature. The resting potential is approximately –72mV and the model is at rest before the stimulation current is applied. Details, model equations and parameters are provided in the supplementary information.

Results

VGSC isoforms activate and inactivate at similar voltage ranges, except for Nav1.8 and Nav1.5

To gain a comparable oversight of biophysics of the VGSCs involved in nociception, we examined Nav1.1, Nav1.2, Nav1.3, Nav1.5, Nav1.6, Nav1.7, Nav1.8 for their voltage dependence of activation and of steady-state fast inactivation (Fig. 1 and 2). Of all channels examined two stand out: Nav1.5 activates and fast inactivates at more hyperpolarized potentials then all other VGSC isoforms (Fig. 1G and 2A/B, Table 2 and S2), whereas Nav1.8 is set apart by its more depolarized activation and fast inactivation (Fig. 1J and 2A/B, Table 2 and S2). The TTX-sensitive VGSCs examined activated at intermediate voltages with Nav1.6 and Nav1.7 being grouped at slightly more hyperpolarized voltages than Nav1.1, Nav1.2 and Nav1.3 (Fig. 1 and 2A/B, Table 2 and S2). Data obtained from fitting conductance-voltage or current-voltage curves to the Boltzmann equation is summarized in Fig. 2 and Table 2. Comparison of the Boltzmann equation fitting results showed differences between the VGSC isoforms in all obtained parameters ($p < 0.0001$ for all ANOVA or Kruskal-Wallis tests).

The overlap between activation and steady-state fast inactivation (SSFI) curves is often referred to as window current (Wang et al. 1996, Magistretti and Alonso 1999, Abriel et al. 2001, Osteen et al. 2017) and some authors refer to it as persistent or ramp current (Blair and Bean 2002, Enomoto et al. 2006, Matsutomi et al. 2006, Vasylyev and Waxman 2012, Estacion and Waxman 2013). The center of the window current of Na1.7 was approximately 5 mV more hyperpolarized than that for the other TTX-s channels (Fig. 1, Table 2). This indicates that in this heterologous expression system Nav1.7 channels are in an open state at more hyperpolarized voltages than the other assumed subthreshold channels Nav1.1, Nav1.2, Nav1.3 and Nav1.6, and thus could contribute to cell depolarization at subthreshold voltages. We did not see a distinct difference in window current sizes nor the fraction of channels remaining open after SSFI between VGSC isoforms: For both measurements, we only saw a slight divergence for Nav1.2/3 and Nav1.8 to smaller or larger window currents, respectively (Fig. 2C/F, Table 2).

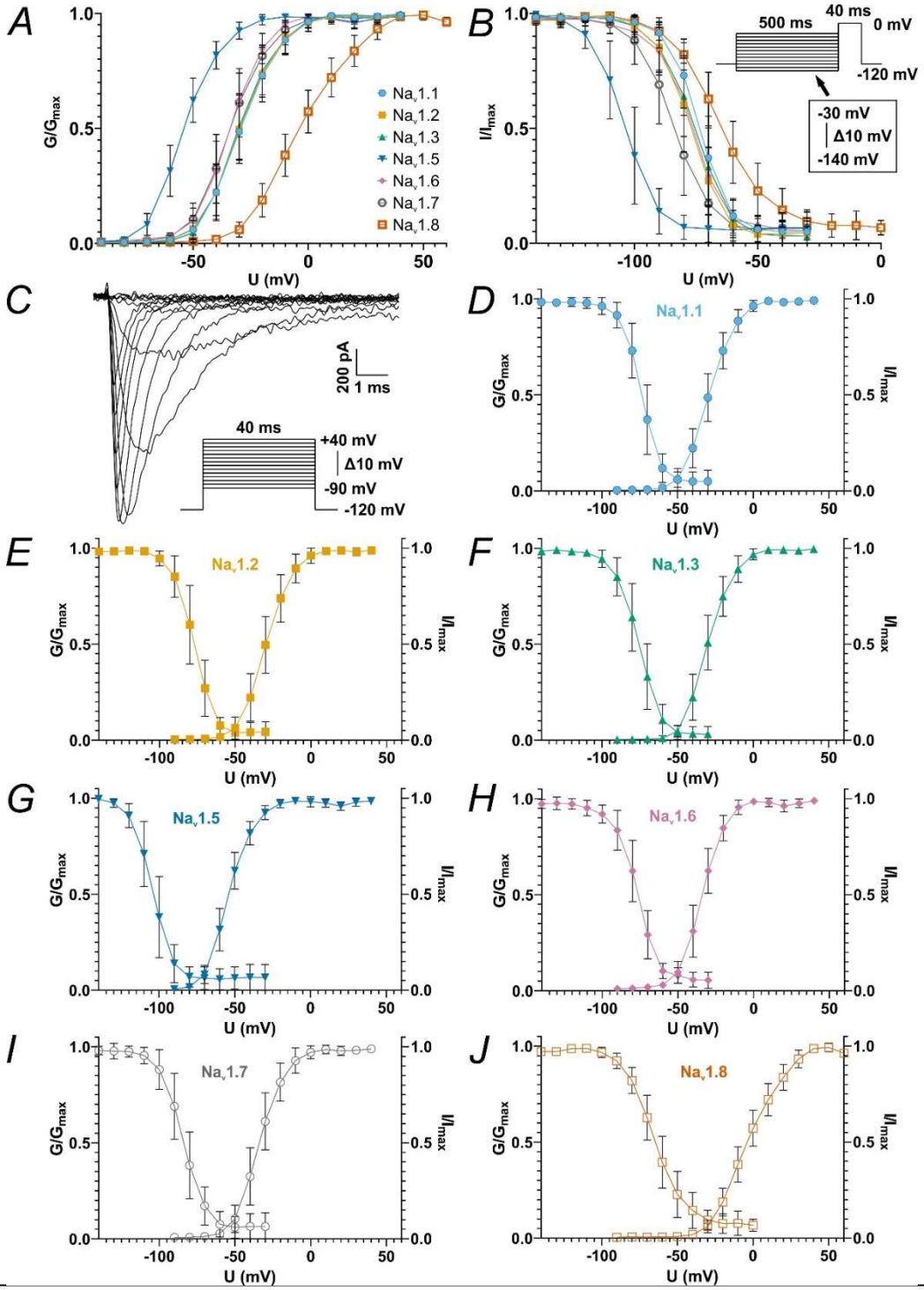

Figure 1: Conductance-voltage or current-voltage relationship of activation and steady-state fast inactivation protocols. *A* overview of all conductance-voltage curves derived from activation measurements. *B* overview of all current-voltage curves derived from steady-state fast inactivation measurements (voltage protocol of steady-state fast inactivation depicted in inlet. Note that for Nav1.8 measurements, most cells were stimulated with a -110 mV to 0 mV voltage range). *C* example traces of Nav1.7 current elicited by the activation protocol (voltage protocol depicted in inlet. Note that for Nav1.8 measurements, most cells were stimulated with a -60 mV to +70 mV voltage range). *D-J* overlay of activation and inactivation curves for Nav1.1 (*D*), Nav1.2 (*E*), Nav1.3 (*F*), Nav1.5 (*G*), Nav1.6 (*H*), Nav1.7 (*I*) and Nav1.8 (*J*). Data is shown as mean ± SD.

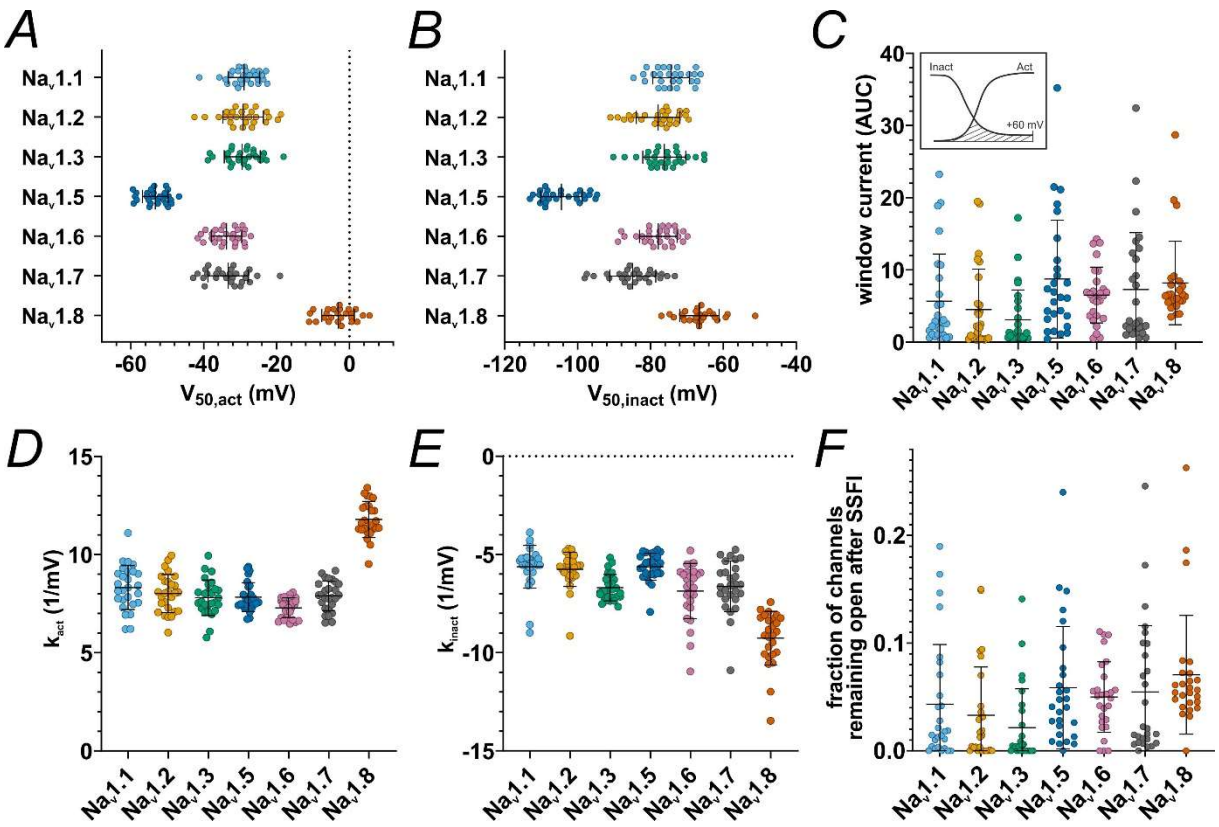

Figure 2: Parameters obtained from fitting activation and steady-state fast inactivation measurements to the Boltzmann equation. *A* V_{50} values gathered from activation Boltzmann fits. *B* V_{50} values gathered from steady-state fast inactivation Boltzmann fits. *C* AUC values underneath the superimposed activation and steady-state fast inactivation Boltzmann fit curves, i.e., the window current. *D* slope values gathered from activation Boltzmann fits. *E* slope values gathered from steady-state fast inactivation Boltzmann fits. *F* bottom values gathered from steady-state fast inactivation Boltzmann fits, indicating the fraction of channels remaining open after complete SSFI. Data is shown as mean ± SD.

Ramp currents and window currents may arise from a similar mechanism only for some VGSC subtypes

Slowly depolarizing voltage ramps induce ramp currents, mimicking the subthreshold phase of an AP. Wild-type ramp currents have been examined for all VGSC isoforms individually (Cummins et al. 1998, Abriel et al. 2001, Herzog et al. 2003, El-Bizri et al. 2011, Power et al. 2012, Estacion and Waxman 2013, DeCaen et al. 2014, Han et al. 2015, Han et al. 2015, Zhang et al. 2017), but not yet in direct comparison between more than two VGSC isoforms. Experimenter-to-experimenter or lab-to-lab variations impair their comparison. Ramp currents are thought to correspond to window currents, i.e., the overlap between activation and steady-state fast inactivation (SSFI) curves (Wang et al. 1996, Magistretti and Alonso 1999, Abriel et al. 2001, Osteen et al. 2017). We set out to compare those two current types in a standardized, comparable manner.

Ramp stimuli evoked a bell-shaped inward current response for all tested VGSC isoforms (Fig. 3), as reported previously (Cummins et al. 1998, Abriel et al. 2001, Herzog et al. 2003, Power et al. 2012, Estacion and Waxman 2013, DeCaen et al. 2014, Han et al. 2015, Zhang et al. 2017). For 6 out of total 27 cells expressing Nav1.3, we observed two peaked ramp currents for slowly depolarizing ramps (i.e., 0.1 mV/ms and partly 0.2 mV/ms) (data not shown) similar to what was reported previously for Nav1.3 (Estacion and Waxman 2013). For the remaining cells and higher ramp rates, only a delayed current decay was observed, potentially corresponding to Nav1.3 persistent current.

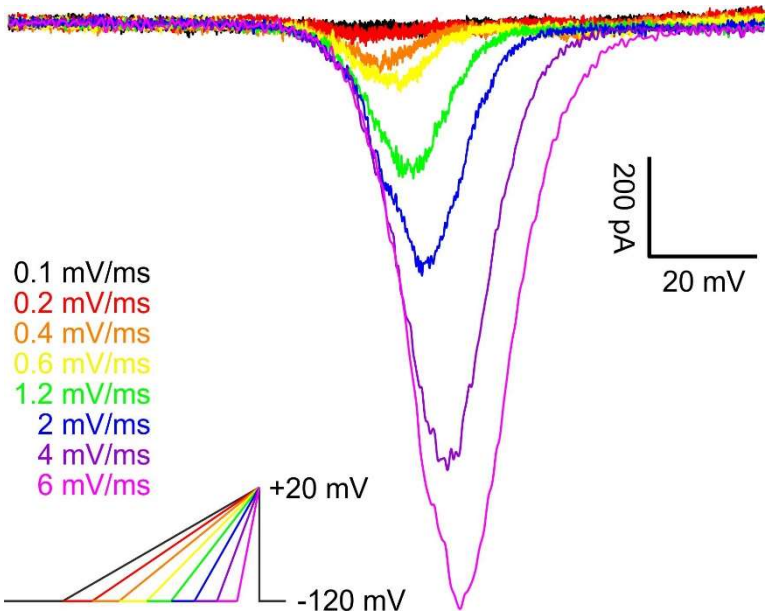

Figure 3: example traces of Nav1.7 ramp currents elicited by slowly depolarizing ramp stimuli (voltage protocol depicted in inlet. Calibrator applies for current traces only).

For maximum inward current (Fig. 4A, Table S3), the ramp rate has more impact on the size of the ramp current than the VGSC isoform: we determined a current difference both between VGSC isoforms ($F(6, 1429) = 153.0$, $p < 0.0001$) and ramp rate ($F(7, 1429) = 974.8$, $p < 0{,}0001$), making up for 9.655% and 71.75% of total variation, respectively. Furthermore, interaction between these terms accounted for 3.325% of total variation ($F(42, 1429) = 7.528$, $p < 0{,}0001$).

Currents for all isoforms increased with steeper ramp stimuli, most likely due to more channels activating before the onset of fast inactivation. As recorded in post-hoc testing (Table S4A), for the lowest ramp rates (i.e., ≤ 0.4 mV/ms), most VGSC isoforms did not differ in maximum inward ramp current, only Nav1.8 elicited higher maximum ramp currents than the other VGSC isoforms. For medium ramp rates (0.6 – 1.2 mV/ms), Nav1.3 and Nav1.8 exceed the other VGSC isoforms, whereas for the highest ramp rates (2 – 6 mV/ms), Nav1.6 and Nav1.7 gradually catch up, leaving Nav1.1, Nav1.2, and Nav1.5 grouped at lower values (Fig. 4A, Table S3).

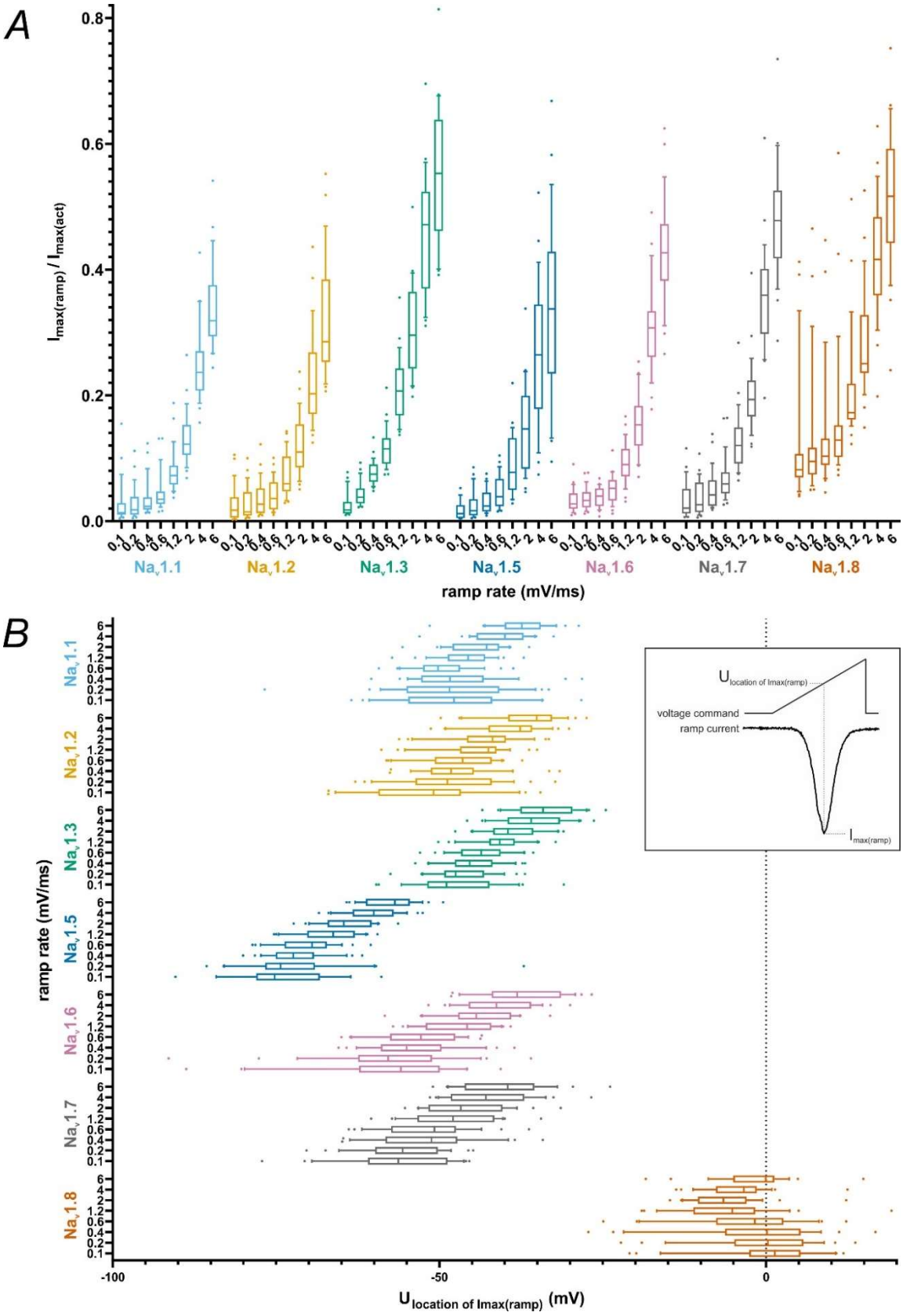

Figure 4: current-voltage parameters obtained from ramp current measurements. *A* maximum inward current from ramp current measurement normalized to maximum inward current from activation measurements. *B* voltage at which the maximum inward current occured during ramp current measurement. Data is shown as box plots with whiskers indicating the 10th and 90th percentile.

Ancillary to the height of the maximum inward ramp current, we examined its voltage dependence (Fig. 4B, Table S3), which was different for the tested VGSC isoforms ($F(6, 1429) = 1748$, $p < 0.0001$; 82.5% of total variation), ramp rate ($F(7, 1429) = 90.15$, $p < 0.0001$; 4.963% of total variation) and their interaction ($F(42, 1429) = 5.17$, $p < 0.0001$; 1.708% of total variation). Using multiple comparison testing (Table S4B), VGSC isoforms showed a distribution matching the results of activation/SSFI V_{50} results and Boltzmann fit intersections for the vast majority, with Nav1.5 and Nav1.8 ramp currents occurring at more hyperpolarized and depolarized voltages, respectively, than all TTXs ramp currents. TTXs channels are grouped at intermediate values, with Nav1.6 and Nav1.7 leaning towards more hyperpolarized values than Nav1.1, Nav1.2, and Nav1.3. For steeper ramps, this effect intensifies, especially for Nav1.7 and Nav1.3.

As a measure of charge added to a cell during slow depolarizations such as the subthreshold phase, we investigated the AUC underneath ramp currents (Fig. 5A, Table S3). Post-hoc testing (Table S5) evidenced that Nav1.8 had larger AUC values than the other VGSC isoforms for all ramp rates. No distinct differences in the AUC between the remaining channel isoforms were observed for lower ramp rates (≤ 0.6 mV/ms). With rising ramp rates, the AUC of Nav1.3, Nav1.5, Nav1.6, and Nav1.7 gradually surpasses the AUC of Nav1.1 and Nav1.2. The AUC is affected by VGSC isoform ($F(6, 1180) = 95.75$, $p < 0{,}0001$; 14.97% of total variation), ramp rate ($F(7, 1180) = 281.6$, $p < 0{,}0001$; 51.38% of total variation) and their interaction ($F(42, 1180) = 1.984$, $p = 0{,}0002$; 2.172% of total variation).

As the window current is assumed to be one underlying mechanism of ramp current generation (Estacion and Waxman 2013), we used Spearman's rank correlation to test for a relationship between window currents and the ramp current AUC (Fig. 5B, Table 3). For Nav1.1, Nav1.2 and Nav1.8, a positive correlation was identified for all ramp rates. For the remaining VGSC isoforms, a positive correlation could only be observed for a few scattered medium ramp rates, indicating that additional mechanisms might play a role for ramp current generation.

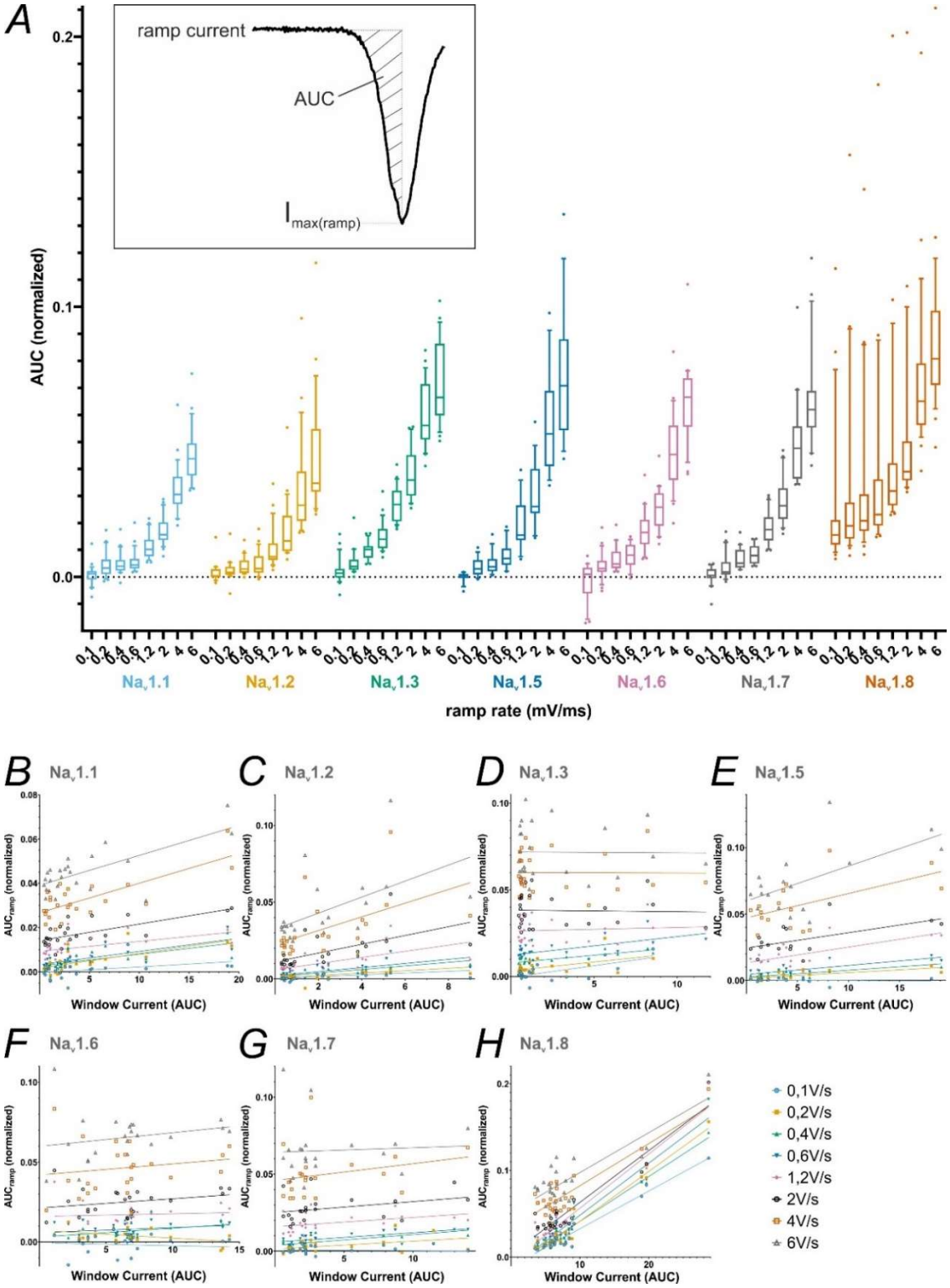

Figure 5: AUC values from ramp current measurements correlate with window current measurements for some VGSC isoforms. *A* AUC values obtained from ramp current measurements, normalized to the maximum inward current from activation measurements for each cell (inlet depicts a schematic example of an AUC underneath a ramp current curve. Note that the AUC was calculated only up to the point of maximum inward current to make up for Nav1.8 ramp currents being cut off at +20 mV). Data is shown as box plots with whiskers indicating the 10th and 90th percentile. *B* correlation between AUC values from ramp current measurements and window current values from activation/steady-state fast inactivation measurements. Data is shown as AUC values plotted against the window current values of the respective cell with a linear regression line for each VGSC

		Nav1.1	Nav1.2	Nav1.3	Nav1.5	Nav1.6	Nav1.7	Nav1.8
0.1	r	0.4904 [0.096; 0.7518]	0.5850 [0.1786; 0.8208]	0.1937 [-0.2497; 0.5699]	0.011 [-0.5561; 0.5711]	-0.0445 [-0.4587; 0.3857]	0.2075 [-0.2718; 0.6044]	0.7222 [0.4213; 0.8799]
	n	24	20	23	13	23	20	22
	p	0.015 (*)	0.0067 (**)	0.3759 (ns)	0.9782 (ns)	0.8403 (ns)	0.38 (ns)	0.0001 (***)
0.2	r	0.7478 [0.4836; 0.8871]	0.6571 [0.3024; 0.8520]	0.3874 [-0.0425; 0.6962]	0.7321 [0.3371; 0.9080]	-0.1575 [-0.5524; 0.2950]	0.3729 [-0.0973; 0.707]	0.8383 [0.6498; 0.9296]
	n	24	21	23	15	22	20	24
	p	< 0.0001 (****)	0.0012 (**)	0.0678 (ns)	0.0027 (**)	0.4838 (ns)	0.1053 (ns)	< 0.0001 (****)
0.4	r	0.8458 [0.6646; 0.9331]	0.8159 [0.5925; 0.9228]	0.5774 [0.2148; 0.8001]	0.4929 [-0.0427; 0.8084]	0.4397 [0.0207; 0.7274]	0.5293 [0.0995; 0.7927]	0.8783 [0.7296; 0.9477]
	n	24	22	24	15	23	20	24
	p	< 0.0001 (****)	< 0.0001 (****)	0.0031 (**)	0.0644 (ns)	0.0358 (*)	0.0164 (*)	< 0.0001 (****)
0.6	r	0.7487 [0.4851; 0.8876]	0.6126 [0.2451; 0.8262]	0.4338 [0.0344; 0.7138]	0.4765 [-0.0412; 0.7925]	0.2125 [-0.2312; 0.5830]	0.6675 [0.3191; 0.857]	0.8009 [0.5788; 0.9124]
	n	24	22	25	16	23	21	24
	p	< 0.0001 (****)	0.0024 (**)	0.0303 (*)	0.0642 (ns)	0.3304 (ns)	0.0009 (***)	< 0.0001 (****)
1.2	r	0.5383 [0.1600; 0.7787]	0.7211 [0.4194; 0.8793]	-0.0038 [-0.4087; 0.4023]	0.4382 [-0.0894; 0.7738]	0.2805 [-0.1852; 0.6434]	0.5468 [0.1372; 0.7966]	0.6769 [0.3741; 0.8493]
	n	24	22	25	16	21	21	25
	p	0.0067 (**)	0.0002 (***)	0.9854 (ns)	0.0913 (ns)	0.2181 (ns)	0.0103 (*)	0.0002 (***)
2	r	0.6896 [0.3857; 0.8585]	0.7132 [0.4059; 0.8756]	0.0131 [-0.3945; 0.4164]	0.3735 [-0.1656; 0.7408]	0.2708 [-0.1718; 0.6224]	0.4312 [-0.0143; 0.7338]	0.6738 [0.3692; 0.8477]
	n	24	22	25	16	23	21	25
	p	0.0002 (***)	0.0002 (***)	0.9505 (ns)	0.1548 (ns)	0.2115 (ns)	0.051 (ns)	0.0002 (***)
4	r	0.5557 [0.1841; 0.7883]	0.6510 [0.3042; 0.8455]	-0.0246 [-0.4259; 0.3847]	0.3824 [-0.1556; 0.7454]	0.2603 [-0.194; 0.6227]	0.3248 [-0.1512; 0.6786]	0.4577 [0.0641; 0.7281]
	n	24	22	25	16	22	20	25
	p	0.0048 (**)	0.001 (**)	0.907 (ns)	0.1447 (ns)	0.242 (ns)	0.1623 (ns)	0.0214 (*)
6	r	0.5296 [0.1481; 0.7739]	0.6002 [0.2266; 0.8199]	0.0077 [-0.3991; 0.4119]	0.3848 [-0.1328; 0.7375]	0.3292 [-0.1204; 0.6667]	0.1744 [-0.3033; 0.5821]	0.47 [0.0797; 0.7354]
	n	24	22	25	17	22	20	25
	p	0.0078 (**)	0.0031 (**)	0.9709 (ns)	0.1281 (ns)	0.1347 (ns)	0.462 (ns)	0.0178 (*)

Table 3: Correlation of window current values from activation/steady-state fast inactivation measurements and AUC values from ramp current measurements. Data is given as Spearman's r [95% CI] with p-values.

VGSC isoforms activate to a differing extent at the subthreshold phase of action potentials

To investigate the subthreshold activity of each VGSC isoform during an AP, we used three pre-recorded APs (AP1, AP2 and AP3, Fig6A-C, Table 1), which differ in their subthreshold properties, their width and size of overshoot. We chose recordings from human iPSC-derived nociceptors (control cells from Meents et al. (2019)) as voltage command and recorded the elicited current response. First, we studied the timepoint within the AP at which the maximum inward current is elicited, for each VGSC isoform (Fig. 6B, 6D, 6F; Table 4), which differed for all AP commands ($p < 0.0001$ for all Kruskal-Wallis tests), as did the maximum inward

current sizes (Fig. 7A-C, Table 4, $p < 0.0001$ for all Kruskal-Wallis tests) and the area under the current response curve (Fig. 7D-F, Table 4; $p < 0.0001$ for all Kruskal-Wallis tests).

	VGSC isoform	$I_{max,totalAP}$/ $I_{max,act}$	timepoint of $I_{max,totalAP}$/ $I_{max,act}$ (ms)	$AUC_{totalAP}$	$I_{max,subthrAP}$/ $I_{max,act}$	$AUC_{subthrAP}$	subthreshold slope (1/ms)	n
AP1	Nav1.1	0,097 ± 0,065	149,7 ± 0,4	0,0015 ± 0,0012	0,0085 ± 0,0064	-0,0015 ± 0,0039	-0,00042 ± 0,001	27
	Nav1.2	0,101 ± 0,052	149,7 ± 0,5	0,0017 ± 0,0048	0,0084 ± 0,0089	-0,0014 ± 0,0059	-0,00023 ± 0,00025	27
	Nav1.3	0,216 ± 0,096	149,5 ± 0,1	0,0048 ± 0,0022	0,0133 ± 0,0081	0,0021 ± 0,0038	-0,00026 ± 0,00023	27
	Nav1.5	0,043 ± 0,047	131,9 ± 34,8	-0,0026 ± 0,019	0,0072 ± 0,0201	-0,0048 ± 0,0229	-0,00043 ± 0,00044	26
	Nav1.6	0,07 ± 0,046	151,9 ± 12,9	0,0021 ± 0,0031	0,0174 ± 0,0168	-0,0014 ± 0,0056	-0,00053 ± 0,00043	27
	Nav1.7	0,098 ± 0,068	147,1 ± 13	0,0025 ± 0,0034	0,0124 ± 0,0089	0,001 ± 0,0054	-0,00035 ± 0,00027	26
	Nav1.8	0,505 ± 0,14	151,5 ± 0,5	0,0081 ± 0,005	0,0062 ± 0,0056	-0,0049 ± 0,0122	-0,00025 ± 0,00032	27
AP2	Nav1.1	0,232 ± 0,1	64,12 ± 0,1	0,0024 ± 0,0033	0,0087 ± 0,0071	0,0011 ± 0,0062	-0,00181 ± 0,00142	27
	Nav1.2	0,216 ± 0,1	64,15 ± 0,14	0,0025 ± 0,0028	0,0086 ± 0,0086	0,0021 ± 0,0055	-0,00188 ± 0,00195	27
	Nav1.3	0,329 ± 0,096	64,14 ± 0,1	0,0041 ± 0,0016	0,015 ± 0,0146	0,0047 ± 0,0073	-0,00231 ± 0,00182	27
	Nav1.5	0,042 ± 0,038	64,25 ± 1,13	0,0018 ± 0,0022	0,0066 ± 0,009	0,0009 ± 0,0081	-0,00179 ± 0,00151	24
	Nav1.6	0,141 ± 0,084	64,14 ± 0,1	0,0014 ± 0,008	0,0099 ± 0,0184	-0,0005 ± 0,0193	-0,00264 ± 0,00151	27
	Nav1.7	0,207 ± 0,121	64,12 ± 0,14	0,0049 ± 0,0041	0,021 ± 0,0157	0,008 ± 0,0115	-0,00368 ± 0,00258	26
	Nav1.8	0,71 ± 0,179	65,49 ± 0,27	0,0104 ± 0,0042	-0,0012 ± 0,0106	-0,0062 ± 0,0141	-0,00147 ± 0,00153	27
AP3	Nav1.1	0,069 ± 0,054	63,13 ± 3,92	0,0071 ± 0,0057	0,0506 ± 0,0216	0,0232 ± 0,0108	-0,00516 ± 0,00221	27
	Nav1.2	0,072 ± 0,053	64,68 ± 3,56	0,0057 ± 0,0062	0,0441 ± 0,0259	0,0175 ± 0,0123	-0,0043 ± 0,00238	27
	Nav1.3	0,196 ± 0,051	63,57 ± 3,13	0,01 ± 0,0078	0,1752 ± 0,0617	0,0767 ± 0,0372	-0,01473 ± 0,00481	27
	Nav1.5	0,065 ± 0,071	66,71 ± 4,13	0,0056 ± 0,0059	0,0107 ± 0,0089	0,0015 ± 0,0064	-0,00164 ± 0,00143	24
	Nav1.6	0,088 ± 0,098	67,71 ± 4,59	0,0086 ± 0,0116	0,0425 ± 0,0199	0,0186 ± 0,0096	-0,00455 ± 0,00254	26
	Nav1.7	0,101 ± 0,058	64,05 ± 4,62	0,0081 ± 0,0073	0,0631 ± 0,0303	0,0305 ± 0,0144	-0,00677 ± 0,00321	26
	Nav1.8	0,36 ± 0,142	71,72 ± 1,9	0,0179 ± 0,013	0,0214 ± 0,0227	-0,0022 ± 0,0118	-0,00261 ± 0,0039	27

Table 4: Descriptive statistics of parameters gathered from AP clamping measurements. Data is shown as mean ± SD.

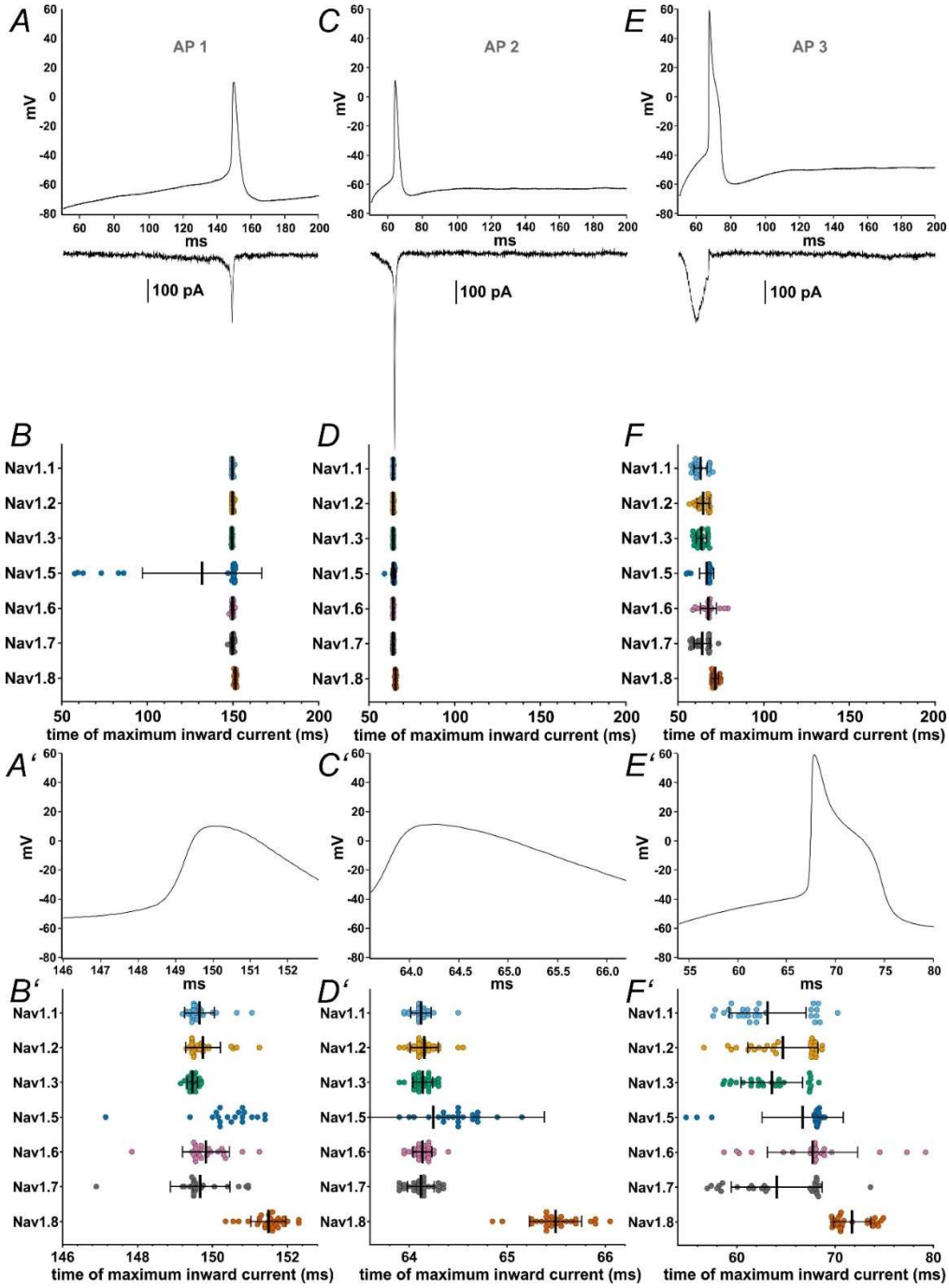

Figure 6: maximum inward current occurs at different timepoints during action potential clamping for each VGSC isoform. *A/C/E* action potential waveforms (AP1 – AP3, respectively) recorded from iPS-derived nociceptors used as voltage commands in AP clamping, with representative current traces, all from the same Nav1.7 cell, charted underneath. *B/D/F* timepoint at which the maximum inward current during the action potential (AP1 – AP3, respectively) occured. *A'-F'* zoomed in depictions of figures *A-F* (excluding the current example traces). Data is shown as mean ± SD.

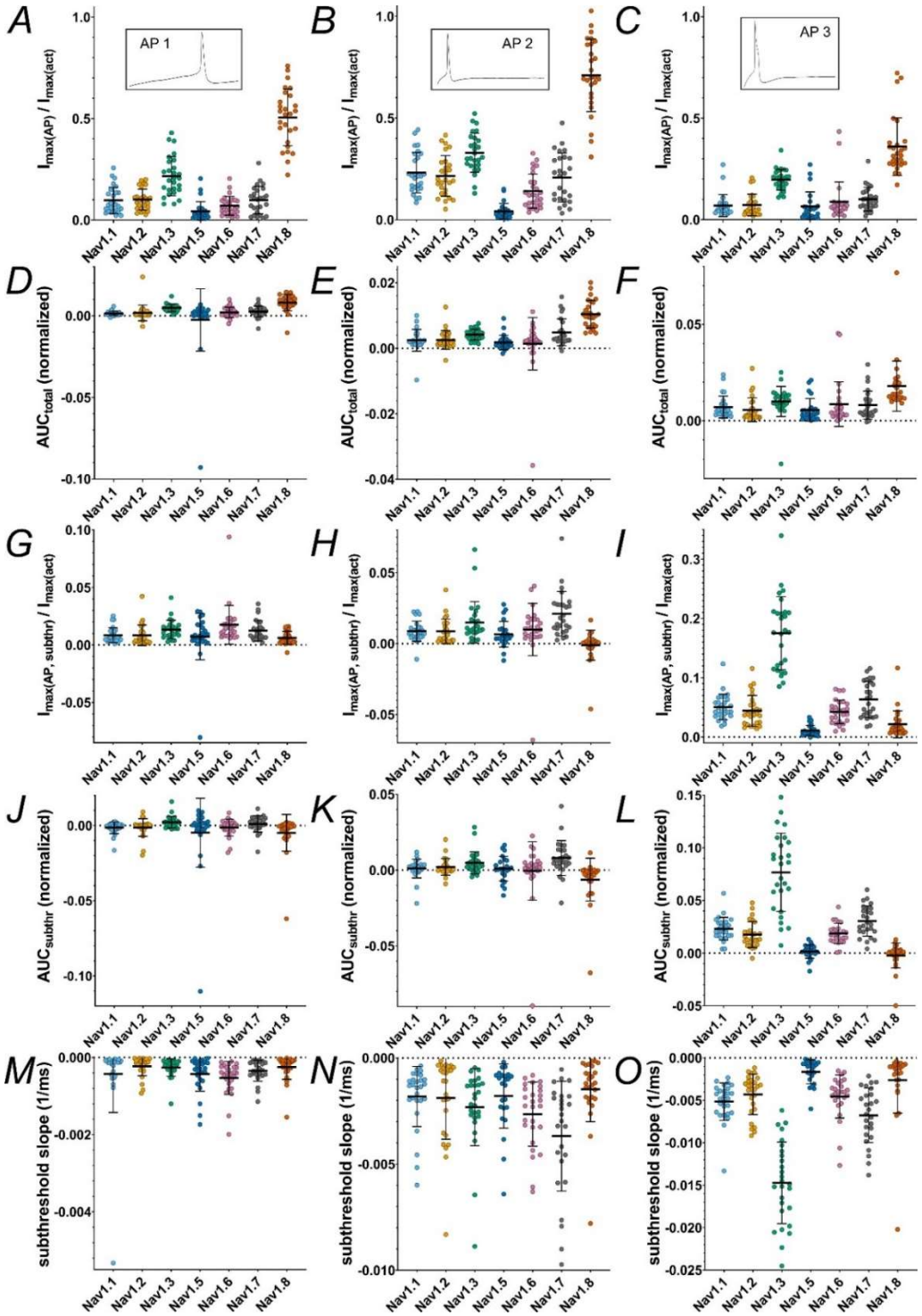

Figure 7: current and AUC parameters obtained from action potential clamping. *A-C* maximum inward current during the total command action potential (AP1-AP3, respectively) normalized to the maximum inward current of activation measurement (inlets indicate the action potential command). *D-F* area under the current response curve to the total command action potential (AP1-AP3, respectively). *G-I* maximum inward current during the subthreshold phase of the command action potential (AP1-AP3, respectively) normalized to the maximum inward current of activation measurement. *J-L* area under the current response curve to the subthreshold phase of the command action potential (AP1-AP3, respectively). *M-O* slope of the inward current measured during the subthreshold phase of the command action potential (AP1-AP3, respectively). Data is shown as mean ± SD.

Multiple comparisons revealed that Nav1.8 currents were elicited at later timepoints than all other VGSC isoforms, namely after the AP peak (Table S6). Nav1.5 currents occurred slightly later within the AP time course as well, whereas Nav1.3 leaned towards earlier timepoints in the subthreshold phase. Note that for all VGSC isoforms, but especially for Nav1.5, Nav1.6, and Nav1.7, data contained several outliers, which we did not exclude, interfering with analysis including determining of the mean (Fig. 6, Table 4). Current sizes and AUC sizes were distributed similarly between the AP commands, with Nav1.8 and Nav1.3 exhibiting larger and Nav1.5 exhibiting slightly lower values for maximum inward current. Nav1.7 showed larger AUC values for AP 2 as well (Fig. 7A-F, Table 4).

Focussing on the subthreshold phase of the APs, results for the maximum inward current, AUC and the inward current slope differed between the VGSC isoforms ($p < 0.0001$ for all Kruskal-Wallis tests except for AP1 subthreshold AUC ($p = 0.0007$) and AP1 subthreshold slope ($p = 0.0004$)).

On average, maximum inward currents increased with increasing subthreshold slope of the AP commands (Fig. 7G-I, Table 4). Post-hoc testing indicates that Nav1.8 and Nav1.5 elicited little to no current during the subthreshold phase, while maximum inward current was higher for Nav1.3 (AP1 and AP3), Nav1.7 (AP2 and AP3), and, for AP1, Nav1.6 (Fig. 7G-I, Table S6). Especially for AP3 with the steepest subthreshold slope, Nav1.3 currents increased drastically (Fig. 7I). The remaining TTXs isoforms had intermediate maximum inward current responses.

A similar pattern of AP evoked current size applied for the subthreshold phase AUC (Fig. 7J-L, Table 4). Nav1.5 and Nav1.8 AUC values remained close to zero for all AP commands (note that negative AUC values occur due to undulation of the current base rate and/or drift). Nav1.7 and Nav1.3 made for larger subthreshold AUC values (the latter particularly for AP3), thereby adding a larger charge to a cell during subthreshold depolarization and potentially alleviating initiation of an AP.

As another measure of channel contribution to subthreshold depolarization, we determined the slope of currents elicited by each VGSC isoform during the subthreshold phase of AP clamping (Fig. 7M-O, Table 4). Steeper subthreshold slopes were documented for Nav1.7 (AP2 and AP3), Nav1.6 (AP1 and AP2), and, with emphasis on AP3, Nav1.3 compared to the other tested channels. In contrast, Nav1.5 and Nav1.8 subthreshold slopes were minor. The data gathered is in line with the assumption that Nav1.8 is mainly activated during the upstroke of a nociceptor AP, while TTXs channels (predominantly Nav1.7, Nav1.6, and – especially for steeper subthreshold depolarizations – Nav1.3) contribute in earlier, subthreshold phases.

In silico simulation suggests significant contribution for Nav1.7 to AP firing in silent and Aδ-nociceptors

To obtain insights in the contribution of the Nav subtypes to the AP we performed in silico experiments. The computational model accounts for the sodium currents of Nav1.1-Nav1.3, Nav1.6-Nav1.8 and a generic potassium current (see Methods). We accounted for the fiber-specific expression patterns of VGSCs quantified in Tavares-Ferreira et al. (2022). The results are depicted in Fig. 8A-E for a putative silent nociceptor and in Fig. 8F-J for an Aδ-fiber. The maximal total sodium, potassium and leak conductivities were chosen to recapitulate the experimentally observed AP morphology. In the simulations the APs were triggered by current injection of 2 µA/cm² throughout the duration of the experiment. To assess the role of a specific VGSC subtype, we removed it from the model and observed the resulting AP changes. According to our simulations Nav1.8 plays an important role for AP overshoot which vanished after its removal (putative silent nociceptor in Fig. 8A; Aδ-fibers in Fig. 8B). Removal of Nav1.1-1.3 and Nav1.6 (at the same time) has no significant impact on the AP of the putative silent nociceptor but reduces the overshoot in the Aδ-fiber (Fig 8C, 8H). The simulations suggest that Nav1.7 is required for the generation of an AP: in both, the putative silent nociceptor and the Aδ-fiber no AP is observed in absence of Nav1.7, simulating *loss-of-function* as it may occur in patients suffering from chronic insensitivity to pain (Fig. 8D, 8I).

Gain-of-function mutations of Nav1.7 linked to inherited pain syndromes often modify channel gating such that during an AP more channels are activated (e.g. hyperpolarized activation for erythromelalgia or impaired fast inactivation for PEPD (Körner and Lampert 2020)). A coarse way to simulate this gain-of-function is to increase the maximal conductance of Nav1.7 in the computer model. Thus, we simulated the putative silent nociceptor and the Aδ-fiber assuming that the quantity of Nav1.7 is doubled. For the putative silent nociceptor this resulted in repetitive APs with positive overshoot (Fig. 8E). In the Aδ-fiber this scenario resulted in repetitive depolarizations not reaching positive potentials (Fig 8J).

We are aware that the removal or addition of a VGSC reduces or increases the maximal total sodium conductance, respectively. For this reason, we simulated the putative silent nociceptor with an increased amount of Nav1.8 (increase by a factor of 3.5), to reach the identical total sodium conductance as for doubling of Nav1.7. In this scenario we observe no repetitive APs. This finding supports the concept that the specific properties of Nav1.7 and not the increase of the total sodium conductance trigger the repetitive activations observed in Fig. 8E. We observed

a similar effect for the Aδ-fiber, where a 3.25-fold increase of Nav1.8 leads to the same total sodium conductance as the doubling of Nav1.7, and no repetitive firing occurred.

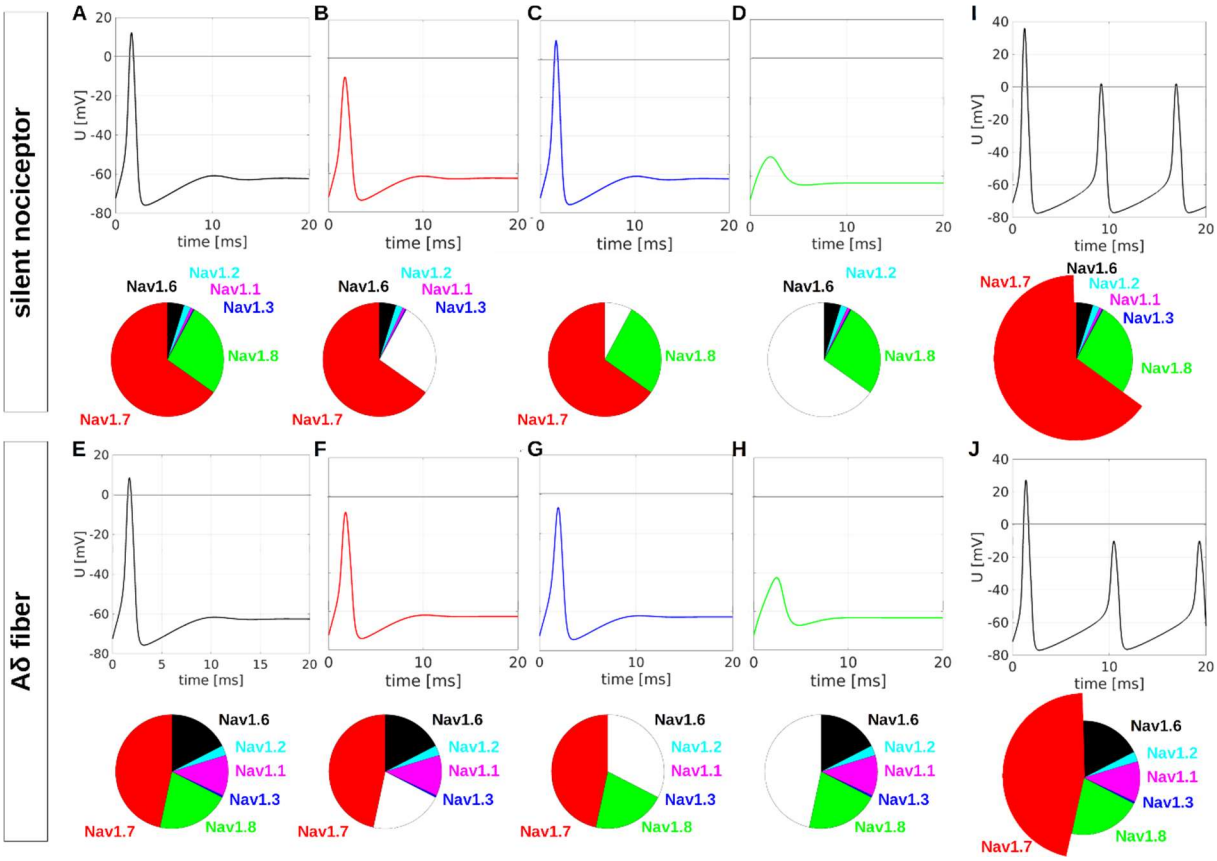

Figure 8: computer simulations of putative silent nociceptor (*A-E*) and Aδ-fiber (*F-J*). The pie charts indicate the abundance of different VGSC subtypes. APs are triggered by an injection of 20uA/cm². *A* and *F* show the APs for the relative abundance of VGSC subtypes quantified in spatial gene expression. *B* and *G* show changes resulting from removal of Nav1.8, *C* and *H* show changes resulting from removal of Nav1.1-1.3 and 1.6. In *D* and *I* Nav1.7 has been removed which results in the loss of the AP. *E* and *J* depict repetitive depolarizations resulting from doubling of Nav1.7. The scenarios *B-D* and *G-I* result in a reduction of the maximal total sodium conductance, the scenarios in *E* and *J* in an increase.

Discussion

In this study, we provide a detailed overview of VGSC isoform biophysics, especially during subthreshold depolarization and modelled their contributions to AP electrogenesis for two types of sensory neurons: silent nociceptors and Aδ-fibers.

Our findings confirmed Nav1.8 contribution to the AP upstroke and its width (Renganathan et al. 2001, Matsutomi et al. 2006, Rush et al. 2007, Vasylyev and Waxman 2012), as it activates and fast-inactivates at more depolarized potentials, elicits large ramp currents at more depolarized potentials and showed little to no subthreshold activity in AP clamping compared to the other VGSCs tested. Knocking out Nav1.8 in the *in silico* experiments led to APs having no overshoot, yet the initiation of the AP was not impeded.

During the subthreshold phases of AP clamping, Nav1.7 showed large AUC values and steeper current slopes compared to the other VGSCs tested. We documented slightly more hyperpolarized voltage dependencies for both SSFI and ramp current measurements than we did for other TTX-s channel isoforms, potentially enabling Nav1.7 to charge a cell at subthreshold voltages. Whether Nav1.7 should be considered a "threshold" or "subthreshold" channel could not be distinguished conclusively.

Our experiments emphasized the importance of Nav1.7 as AP initiator, also since knocking out or enhancing Nav1.7 *in silico* led to omitted or multiple APs, respectively. This resembles putative *loss*- and *gain-of-function* pathophysiology that is attributed to Nav1.7 channelopathies (Dib-Hajj et al. 2005, Cox et al. 2006, Faber et al. 2012, Bennett et al. 2019, McDermott et al. 2019).

Analysis of the remaining VGSC isoforms' contribution to AP subthreshold phase led to more nuanced results. Out of the remaining TTX-s channels, which all had their voltage dependence of activation, SSFI and ramp currents at subthreshold voltages, only Nav1.6 stood out to some extent, having higher maximum inward currents and steeper current slopes during the subthreshold phase of AP clamping. Also, leaving out these channels during the *in silico* testing had no noticeable effect on AP morphology, likely because of their minor share in the spatial transcriptomics-derived expression patterns used in the model (Tavares-Ferreira et al. 2022).

Nav1.5 played no major role during subthreshold AP clamping, while it is also not expressed in C-fibers and only marginally in Aδ-fibers (Tavares-Ferreira et al. 2022). Its role during development needs to be investigated in more detail in follow-up studies (Renganathan et al. 2002).

We documented large Nav1.3 currents during clamping of an AP with steep subthreshold voltage slope (AP3), and – consistent with literature – during steeper voltage ramps (Cummins et al. 2001). This might play a role in in neuropathic pain, as some studies suggest that Nav1.3 is upregulated in spinal cord or peripheral nerve injuries in rodents and therefore might cause an increased excitability (Hains et al. 2003, Hains et al. 2004, Lampert et al. 2006). Other studies present more ambiguous or even contradictory results, e.g., Nav1.3 knockout mice did not show lowered pain thresholds after nerve injury than wildtype mice (Lindia et al. 2005, Nassar et al. 2006). The underlying causes of neuropathic pain are still under investigation.

We observed a correlation between window current and ramp AUC measurements to some extent, especially for Nav1.1, Nav1.2, and Nav1.8. As this was partly not the case for the other channels, we suppose that additional factors such as persistent current play into ramp current formation, as suggested in literature (Estacion and Waxman 2013). As ramp currents are a very simplified model of the subthreshold phase of an AP, window currents should be interpreted with caution in terms of excitability investigations.

For some experiments, e.g., voltage dependence of AP clamping, analysis was impaired by several outliers, which we did not exclude. When reviewing raw data, several of these outliers appeared to result of measurement artifacts, so that it might be worthwhile to amend an outlier analysis. To compensate for outliers destabilizing statistical results, usage of high-throughput, automated patch-clamp systems could also be considered, as they offer a time-efficient method to gather large data sets (Kriegeskorte et al. 2023, Thompson et al. 2023).

For Nav1.3 and Nav1.6 measurements in this study, we used rodent channel isoforms. As reported previously, pronounced biophysical differences such as larger persistent or ramp currents can occur between VGSC isoforms from different mammalian species (Tan and Soderlund 2009, Han et al. 2015). Hence, complementary measurements with human channel isoforms are desirable.

Nav1.9 is a key player in membrane potential modulation of PNS neurons. As we did not include Nav1.9 in this study due to a lack of Nav1.9 expression in heterologous systems, further investigation is needed either in finding new and practicable ways to examine Nav1.9 channels in heterologous expression systems, or its measurements in primary neurons.

Heterologous expression systems bear their own interpretation pitfalls, as they do not resemble the complex environment of primary neurons, e.g., regarding cell morphology, intercellular contacts, or membrane protein interactions. VGSC isoforms have been studied to have different gating behavior when expressed in different expression systems (Cummins et al. 2001, Rush et

al. 2006, Tan and Soderlund 2009, Zhang et al. 2017). Future studies in expression systems closer to human peripheral sensory neurons such as rodent or even human DRG neurons, could give a better insight into the channels biophysics *in vivo*. Alternatively, nociceptors derived from human induced pluripotent stem cells offer the possibility to investigate ion channels in an adaption of their native environment (Meents et al. 2019, Mis et al. 2019, Namer et al. 2019). This could also make up for the fact that we included neither β-subunits into our measurements nor did we check for channel dimerization, both of which have shown to alter biophysical properties of VGSCs (Brackenbury and Isom 2011, Chahine and O'Leary 2011, Clatot et al. 2017, Rühlmann et al. 2020).

In applying the mRNA expression data from the human DRG spatial transcriptomics study (Tavares-Ferreira et al. 2022) to allocate the maximal channel conductance in our computational model, we limit transferability, since expressed mRNA does not indicate sufficiently that the respective channel will be expressed on the cell surface and is fully functional. Alternative splicing, trafficking or membrane turnover are just some factors that may impact channel translation from RNA to functional protein in the membrane. A promising solution to these problems are single-cell transcriptomics, such as Patch-seq, which offer the ability to link expression data to cell physiology (Lipovsek et al. 2021, Körner et al. 2022). Furthermore, since expression data is gathered at the cell soma, only limited assumptions can be made for small nerve fibers, e.g., in the human skin.

Note that computational models are simplifications of the real world and therefore must be handled cautiously, especially when model complexity suggests the opposite. For example, VGSC data is usually gathered at room temperature, and temperature dependence of VGSCs varies for each channel subtype and recorded voltages (Kriegeskorte et al. 2023). Thus, most computational models published in the recent years do not account for temperature, since this would require additional experimental data and re-parametrization of the models (Almog and Korngreen 2016). Our computational model is a single-compartment model, and the ion channels are modeled with modified Hodgkin-Huxley dynamics. To further study the VGSC influence on the action potential generation, the VGSC subtypes could be implemented in a morphologically detailed C-fiber or Aδ-fiber model (Tigerholm et al. 2014, Tigerholm et al. 2019). The in silico experimental results in this study show that Nav1.7 initiates the AP while Nav1.8 generates the AP. This is consistent with previous in-silico modeling results (Tigerholm et al. 2014, Tigerholm et al. 2019). However, repetitive firing has previously been associated with the Nav1.8 current (Tigerholm et al. 2020, Verma et al. 2020). This is not consistent with the results of this study, which shows that repetitive firing may originate from the Nav1.7

current. One possible explanation for the different results can originate from the different resting membrane potentials of the *in silico* models. Since the model in this study has more hyperpolarized resting membrane potentials, it can increase the influence of the TTX-sensitive currents compared to the TTX-resistant currents (Blair and Bean 2002, Tigerholm et al. 2015).

For now, this study provided a broadly based groundwork for future comparative studies of VGSC isoforms, their biophysics and interaction with each other. By feeding our measurements into a computational model, we generated an *in silico* tool to test hypotheses and on that basis to plan new experiments. After further refinement, extension, and validation, such *in silico* tools could be used e.g., for disease modelling or pharmacodynamic modeling. This may also prove useful when developing new potential analgesics such as specific channel blockers or when optimizing therapy schemes for chronic pain.

Additional information

Data availability

All data gathered in this study and all analysis procedures used are available from the corresponding author upon reasonable request.

Disclosures/Competing interests

The authors declare no competing financial interests/no conflicts of interest with the contents of this article. A.L. has an unrelated research agreement with Grunenthal. A.L. receives counseling fees from Grunenthal.

Authors contribution

P. A. K.: wrote the initial draft of the manuscript, planned and designed experiments, performed electrophysiological experiments, analyzed and interpreted the data, validated and visualised the data.

T. S.: developed and implemented modified gating equations for the Hodgkin Huley model and parameterized them based on the experimental data, performed *in silico* experiments, critically revised the manuscript.

J. T.: interpreted the data, critically revised the manuscript.

A. M.: interpreted the data, critically revised the manuscript.

B. N.: interpreted the data, critically revised the manuscript.

A. L.: conceived the study, planned and designed experiments, interpreted the data, provided funding and resources, administered and supervised the project, critically revised the manuscript.

Funding/Grants

This work was funded by the Deutsche Forschungsgemeinschaft (DFG, German Research Foundation 363055819/GRK2415 Mechanobiology of 3D epithelial tissues (ME3T); 368482240/GRK2416, MultiSenses-MultiScales). A.L. and B.N. are supported by a grant from the Interdisciplinary Center for Clinical Research within the Faculty of Medicine at the RWTH Aachen University (IZKF TN1-1/IA 532001).

Acknowledgements

We thank Brigitte Hoch, Raya A. Bott, and Petra Hautvast for their excellent technical support (cell culture, molecular biology, electrophysiology). We thank Jannis Körner, Sophia

Kriegeskorte and Jannis E. Meents for their thoughtful discussions as well as Jannis E. Meents for providing the AP stimuli used in this study.

Abbreviations

The following abbreviations are used: *AP* action potential, *AUC* area under the curve, *CIP* congenital insensitivity to pain, *CNS* central nervous system, *DMEM* Dulbecco's modified Eagle medium, *DRG* dorsal root ganglion, *ECS* extracellular solution, E_{rev} reversal potential, *FBS* fetal bovine serum, G_{Na} sodium conductance, $G_{Na,max}$ maximum sodium conductance, *G418* Geneticin disulphate, *ICS* intracellular solution, *IEM* inherited erythromelalgia, I_{Na} inward sodium current, $I_{Na,max}$ maximum inward sodium current *iPS* induced pluripotent stem cells, *k* slope factor, *LJP* liquid junction potential, *PEPD* paroxysmal extreme pain disorder, *PNS* peripheral nervous system, *RMP* resting membrane potential, R_{pip} pipette tip resistance, R_s series resistance, R_{seal} seal resistance, *SD* standard deviation, *SFN* small fiber neuropathy, *SSFI* steady-state fast inactivation, *TTX* tetrodotoxin, *TTXr* TTX-resistant, *TTXs* TTX-sensitive, *VGSC* voltage-gated sodium channel, V_h holding potential, V_m membrane potential, V_{50} membrane potential at half-maximal channel (in)activation.

Supporting Information/Supplements

You can find the supporting information files here: http://www.thomas-stiehl.de/Preprints.html

References

Abriel, H., C. Cabo, X. H. Wehrens, I. Rivolta, H. K. Motoike, M. Memmi, C. Napolitano, S. G. Priori and R. S. Kass (2001). "Novel arrhythmogenic mechanism revealed by a long-QT syndrome mutation in the cardiac Na(+) channel." Circ Res **88**(7): 740-745.
Ahern, C. A., J. Payandeh, F. Bosmans and B. Chanda (2016). "The hitchhiker's guide to the voltage-gated sodium channel galaxy." J Gen Physiol **147**(1): 1-24.
Almog, M. and A. Korngreen (2016). "Is realistic neuronal modeling realistic?" J Neurophysiol **116**(5): 2180-2209.
Bennett, D. L., A. J. Clark, J. Huang, S. G. Waxman and S. D. Dib-Hajj (2019). "The Role of Voltage-Gated Sodium Channels in Pain Signaling." Physiol Rev **99**(2): 1079-1151.
Bennett, D. L. and C. G. Woods (2014). "Painful and painless channelopathies." Lancet Neurol **13**(6): 587-599.
Bhattacharjee, A., Y. Xiao, Z. Pei and T. R. Cummins (2018). Specialized Sodium Channels in Pain Transmission, Oxford University Press.
Blair, N. T. and B. P. Bean (2002). "Roles of tetrodotoxin (TTX)-sensitive Na+ current, TTX-resistant Na+ current, and Ca2+ current in the action potentials of nociceptive sensory neurons." J Neurosci **22**(23): 10277-10290.
Brackenbury, W. J. and L. L. Isom (2011). "Na Channel β Subunits: Overachievers of the Ion Channel Family." Front Pharmacol **2**: 53.

Brouwer, B. A., I. S. Merkies, M. M. Gerrits, S. G. Waxman, J. G. Hoeijmakers and C. G. Faber (2014). "Painful neuropathies: the emerging role of sodium channelopathies." J Peripher Nerv Syst **19**(2): 53-65.
Catterall, W. A., A. L. Goldin and S. G. Waxman (2005). "International Union of Pharmacology. XLVII. Nomenclature and structure-function relationships of voltage-gated sodium channels." Pharmacol Rev **57**(4): 397-409.
Chahine, M. and M. E. O'Leary (2011). "Regulatory Role of Voltage-Gated Na Channel β Subunits in Sensory Neurons." Front Pharmacol **2**: 70.
Clatot, J., M. Hoshi, X. Wan, H. Liu, A. Jain, K. Shinlapawittayatorn, C. Marionneau, E. Ficker, T. Ha and I. Deschênes (2017). "Voltage-gated sodium channels assemble and gate as dimers." Nat Commun **8**(1): 2077.
Cox, J. J., F. Reimann, A. K. Nicholas, G. Thornton, E. Roberts, K. Springell, G. Karbani, H. Jafri, J. Mannan, Y. Raashid, L. Al-Gazali, H. Hamamy, E. M. Valente, S. Gorman, R. Williams, D. P. McHale, J. N. Wood, F. M. Gribble and C. G. Woods (2006). "An SCN9A channelopathy causes congenital inability to experience pain." Nature **444**(7121): 894-898.
Cummins, T. R., F. Aglieco, M. Renganathan, R. I. Herzog, S. D. Dib-Hajj and S. G. Waxman (2001). "Nav1.3 sodium channels: rapid repriming and slow closed-state inactivation display quantitative differences after expression in a mammalian cell line and in spinal sensory neurons." The Journal of neuroscience : the official journal of the Society for Neuroscience **21**(16): 5952-5961.
Cummins, T. R., J. R. Howe and S. G. Waxman (1998). "Slow closed-state inactivation: a novel mechanism underlying ramp currents in cells expressing the hNE/PN1 sodium channel." J Neurosci **18**(23): 9607-9619.
de Lera Ruiz, M. and R. L. Kraus (2015). "Voltage-Gated Sodium Channels: Structure, Function, Pharmacology, and Clinical Indications." Journal of Medicinal Chemistry **58**(18): 7093-7118.
DeCaen, P. G., Y. Takahashi, T. A. Krulwich, M. Ito and D. E. Clapham (2014). "Ionic selectivity and thermal adaptations within the voltage-gated sodium channel family of alkaliphilic Bacillus." eLife **3**: e04387.
Dib-Hajj, S. D., T. R. Cummins, J. A. Black and S. G. Waxman (2010). "Sodium channels in normal and pathological pain." Annu Rev Neurosci **33**: 325-347.
Dib-Hajj, S. D., P. Geha and S. G. Waxman (2017). "Sodium channels in pain disorders: pathophysiology and prospects for treatment." Pain **158 Suppl 1**(Suppl 1): S97-s107.
Dib-Hajj, S. D., A. M. Rush, T. R. Cummins, F. M. Hisama, S. Novella, L. Tyrrell, L. Marshall and S. G. Waxman (2005). "Gain-of-function mutation in Nav1.7 in familial erythromelalgia induces bursting of sensory neurons." Brain **128**(Pt 8): 1847-1854.
Eberhardt, E., S. Havlicek, D. Schmidt, Andrea S. Link, C. Neacsu, Z. Kohl, M. Hampl, Andreas M. Kist, A. Klinger, C. Nau, J. Schüttler, C. Alzheimer, J. Winkler, B. Namer, B. Winner and A. Lampert (2015). "Pattern of Functional TTX-Resistant Sodium Channels Reveals a Developmental Stage of Human iPSC- and ESC-Derived Nociceptors." Stem Cell Reports **5**(3): 305-313.
El-Bizri, N., K. M. Kahlig, J. C. Shyrock, J. A. L. George, L. Belardinelli and S. Rajamani (2011). "Ranolazine block of human Nav1.4 sodium channels and paramyotonia congenita mutants." Channels **5**(2): 161-172.
Enomoto, A., J. M. Han, C.-F. Hsiao, N. Wu and S. H. Chandler (2006). "Participation of sodium currents in burst generation and control of membrane excitability in mesencephalic trigeminal neurons." The Journal of neuroscience : the official journal of the Society for Neuroscience **26**(13): 3412-3422.
Estacion, M. and S. G. Waxman (2013). "The response of NaV1.3 sodium channels to ramp stimuli: multiple components and mechanisms." Journal of Neurophysiology **109**(2): 306-314.
Faber, C. G., J. G. Hoeijmakers, H. S. Ahn, X. Cheng, C. Han, J. S. Choi, M. Estacion, G. Lauria, E. K. Vanhoutte, M. M. Gerrits, S. Dib-Hajj, J. P. Drenth, S. G. Waxman and I. S. Merkies (2012). "Gain of function Nanu1.7 mutations in idiopathic small fiber neuropathy." Ann Neurol **71**(1): 26-39.

Faber, C. G., J. G. Hoeijmakers, H. S. Ahn, X. Cheng, C. Han, J. S. Choi, M. Estacion, G. Lauria, E. K. Vanhoutte, M. M. Gerrits, S. Dib-Hajj, J. P. Drenth, S. G. Waxman and I. S. Merkies (2012). "Gain of function Nav1.7 mutations in idiopathic small fiber neuropathy." Ann Neurol **71**(1): 26-39.
Felts, P. A., S. Yokoyama, S. Dib-Hajj, J. A. Black and S. G. Waxman (1997). "Sodium channel alpha-subunit mRNAs I, II, III, NaG, Na6 and hNE (PN1): different expression patterns in developing rat nervous system." Brain Res Mol Brain Res **45**(1): 71-82.
Fertleman, C. R., M. D. Baker, K. A. Parker, S. Moffatt, F. V. Elmslie, B. Abrahamsen, J. Ostman, N. Klugbauer, J. N. Wood, R. M. Gardiner and M. Rees (2006). "SCN9A mutations in paroxysmal extreme pain disorder: allelic variants underlie distinct channel defects and phenotypes." Neuron **52**(5): 767-774.
Fukuoka, T., K. Kobayashi, H. Yamanaka, K. Obata, Y. Dai and K. Noguchi (2008). "Comparative study of the distribution of the alpha-subunits of voltage-gated sodium channels in normal and axotomized rat dorsal root ganglion neurons." J Comp Neurol **510**(2): 188-206.
Goodwin, G. and S. B. McMahon (2021). "The physiological function of different voltage-gated sodium channels in pain." Nature Reviews Neuroscience **22**(5): 263-274.
Goral, R. O., E. Leipold, E. Nematian-Ardestani and S. H. Heinemann (2015). "Heterologous expression of NaV1.9 chimeras in various cell systems." Pflugers Arch **467**(12): 2423-2435.
Hains, B. C., J. P. Klein, C. Y. Saab, M. J. Craner, J. A. Black and S. G. Waxman (2003). "Upregulation of sodium channel Nav1.3 and functional involvement in neuronal hyperexcitability associated with central neuropathic pain after spinal cord injury." J Neurosci **23**(26): 8881-8892.
Hains, B. C., C. Y. Saab, J. P. Klein, M. J. Craner and S. G. Waxman (2004). "Altered sodium channel expression in second-order spinal sensory neurons contributes to pain after peripheral nerve injury." J Neurosci **24**(20): 4832-4839.
Han, C., M. Estacion, J. Huang, D. Vasylyev, P. Zhao, S. D. Dib-Hajj and S. G. Waxman (2015). "Human Na(v)1.8: enhanced persistent and ramp currents contribute to distinct firing properties of human DRG neurons." J Neurophysiol **113**(9): 3172-3185.
Han, C., Y. Yang, B. T. A. de Greef, J. G. J. Hoeijmakers, M. M. Gerrits, C. Verhamme, J. Qu, G. Lauria, I. S. J. Merkies, C. G. Faber, S. D. Dib-Hajj and S. G. Waxman (2015). "The Domain II S4-S5 Linker in Nav1.9: A Missense Mutation Enhances Activation, Impairs Fast Inactivation, and Produces Human Painful Neuropathy." NeuroMolecular Medicine **17**(2): 158-169.
Herzog, R. I., T. R. Cummins, F. Ghassemi, S. D. Dib-Hajj and S. G. Waxman (2003). "Distinct repriming and closed-state inactivation kinetics of Nav1.6 and Nav1.7 sodium channels in mouse spinal sensory neurons." The Journal of physiology **551**(Pt 3): 741-750.
Herzog, R. I., T. R. Cummins and S. G. Waxman (2001). "Persistent TTX-resistant Na+ current affects resting potential and response to depolarization in simulated spinal sensory neurons." J Neurophysiol **86**(3): 1351-1364.
Hodgkin, A. L. and A. F. Huxley (1952). "A quantitative description of membrane current and its application to conduction and excitation in nerve." The Journal of Physiology **117**(4): 500-544.
Hoeijmakers, J. G. J., I. S. J. Merkies, M. M. Gerrits, S. G. Waxman and C. G. Faber (2012). "Genetic aspects of sodium channelopathy in small fiber neuropathy." Clinical Genetics **82**(4): 351-358.
Huang, J., Y. Yang, P. Zhao, M. M. Gerrits, J. G. J. Hoeijmakers, K. Bekelaar, I. S. J. Merkies, C. G. Faber, S. D. Dib-Hajj and S. G. Waxman (2013). "Small-fiber neuropathy Nav1.8 mutation shifts activation to hyperpolarized potentials and increases excitability of dorsal root ganglion neurons." The Journal of neuroscience : the official journal of the Society for Neuroscience **33**(35): 14087-14097.
Jarecki, B. W., P. L. Sheets, J. O. Jackson, 2nd and T. R. Cummins (2008). "Paroxysmal extreme pain disorder mutations within the D3/S4-S5 linker of Nav1.7 cause moderate destabilization of fast inactivation." J Physiol **586**(17): 4137-4153.
Kleggetveit, I. P., B. Namer, R. Schmidt, T. Helås, M. Rückel, K. Ørstavik, M. Schmelz and E. Jørum (2012). "High spontaneous activity of C-nociceptors in painful polyneuropathy." Pain **153**(10): 2040-2047.

Klugbauer, N., L. Lacinova, V. Flockerzi and F. Hofmann (1995). "Structure and functional expression of a new member of the tetrodotoxin-sensitive voltage-activated sodium channel family from human neuroendocrine cells." Embo j **14**(6): 1084-1090.
Körner, J., N. Haag, I. Kurth and A. Lampert (2022). "Genetics meets function in sodium channel-related pain disorders." **28**(2): 67-75.
Körner, J. and A. Lampert (2020). "Sodium channels."
Körner, J., J. Meents, J. P. Machtens and A. Lampert (2018). "β1 subunit stabilises sodium channel Nav1.7 against mechanical stress." J Physiol **596**(12): 2433-2445.
Kriegeskorte, S., R. Bott, M. Hampl, A. Korngreen, R. Hausmann and A. Lampert (2023). "Cold and warmth intensify pain-linked sodium channel gating effects and persistent currents." J Gen Physiol **155**(9).
Laezza, F., A. Lampert, M. A. Kozel, B. R. Gerber, A. M. Rush, J. M. Nerbonne, S. G. Waxman, S. D. Dib-Hajj and D. M. Ornitz (2009). "FGF14 N-terminal splice variants differentially modulate Nav1.2 and Nav1.6-encoded sodium channels." Mol Cell Neurosci **42**(2): 90-101.
Lampert, A., B. C. Hains and S. G. Waxman (2006). "Upregulation of persistent and ramp sodium current in dorsal horn neurons after spinal cord injury." Experimental Brain Research **174**(4): 660-666.
Lampert, A., A. O. O'Reilly, P. Reeh and A. Leffler (2010). "Sodium channelopathies and pain." Pflugers Arch **460**(2): 249-263.
Lee, J., S. Kim, H.-m. Kim, H. J. Kim and F. H. Yu (2019). "NaV1.6 and NaV1.7 channels are major endogenous voltage-gated sodium channels in ND7/23 cells." PLOS ONE **14**(8): e0221156.
Leipold, E., L. Liebmann, G. C. Korenke, T. Heinrich, S. Gießelmann, J. Baets, M. Ebbinghaus, R. O. Goral, T. Stödberg, J. C. Hennings, M. Bergmann, J. Altmüller, H. Thiele, A. Wetzel, P. Nürnberg, V. Timmerman, P. De Jonghe, R. Blum, H.-G. Schaible, J. Weis, S. H. Heinemann, C. A. Hübner and I. Kurth (2013). "A de novo gain-of-function mutation in SCN11A causes loss of pain perception." Nature Genetics **45**: 1399.
Liang, L., S. Fazel Darbandi, S. Pochareddy, F. O. Gulden, M. C. Gilson, B. K. Sheppard, A. Sahagun, J. Y. An, D. M. Werling, J. L. R. Rubenstein, N. Sestan, K. J. Bender and S. J. Sanders (2021). "Developmental dynamics of voltage-gated sodium channel isoform expression in the human and mouse brain." Genome Med **13**(1): 135.
Lindia, J. A., M. G. Köhler, W. J. Martin and C. Abbadie (2005). "Relationship between sodium channel NaV1.3 expression and neuropathic pain behavior in rats." Pain **117**(1-2): 145-153.
Lipovsek, M., C. Bardy, C. R. Cadwell, K. Hadley, D. Kobak and S. J. Tripathy (2021). "Patch-seq: Past, Present, and Future." J Neurosci **41**(5): 937-946.
Magistretti, J. and A. Alonso (1999). "Biophysical properties and slow voltage-dependent inactivation of a sustained sodium current in entorhinal cortex layer-II principal neurons: a whole-cell and single-channel study." The Journal of general physiology **114**(4): 491-509.
Maingret, F., B. Coste, F. Padilla, N. Clerc, M. Crest, S. M. Korogod and P. Delmas (2008). "Inflammatory mediators increase Nav1.9 current and excitability in nociceptors through a coincident detection mechanism." J Gen Physiol **131**(3): 211-225.
Matsutomi, T., C. Nakamoto, T. Zheng, J. Kakimura and N. Ogata (2006). "Multiple types of Na(+) currents mediate action potential electrogenesis in small neurons of mouse dorsal root ganglia." Pflugers Arch **453**(1): 83-96.
McDermott, L. A., G. A. Weir, A. C. Themistocleous, A. R. Segerdahl, I. Blesneac, G. Baskozos, A. J. Clark, V. Millar, L. J. Peck, D. Ebner, I. Tracey, J. Serra and D. L. Bennett (2019). "Defining the Functional Role of NaV1.7 in Human Nociception." Neuron **101**(5): 905-919.e908.
Meents, J. E., E. Bressan, S. Sontag, A. Foerster, P. Hautvast, C. Rosseler, M. Hampl, H. Schuler, R. Goetzke, T. K. C. Le, I. P. Kleggetveit, K. Le Cann, C. Kerth, A. M. Rush, M. Rogers, Z. Kohl, M. Schmelz, W. Wagner, E. Jorum, B. Namer, B. Winner, M. Zenke and A. Lampert (2019). "The role of Nav1.7 in human nociceptors: insights from human induced pluripotent stem cell-derived sensory neurons of erythromelalgia patients." Pain **160**(6): 1327-1341.

Meents, J. E. and A. Lampert (2016). Studying Sodium Channel Gating in Heterologous Expression Systems. Advanced Patch-Clamp Analysis for Neuroscientists. A. Korngreen. New York, NY, Springer New York: 37-65.
Mis, M. A., Y. Yang, B. S. Tanaka, C. Gomis-Perez, S. Liu, F. Dib-Hajj, T. Adi, R. Garcia-Milian, B. R. Schulman, S. D. Dib-Hajj and S. G. Waxman (2019). "Resilience to Pain: A Peripheral Component Identified Using Induced Pluripotent Stem Cells and Dynamic Clamp." J Neurosci **39**(3): 382-392.
Namer, B., D. Schmidt, E. Eberhardt, M. Maroni, E. Dorfmeister, I. P. Kleggetveit, L. Kaluza, J. Meents, A. Gerlach, Z. Lin, A. Winterpacht, E. Dragicevic, Z. Kohl, J. Schuttler, I. Kurth, T. Warncke, E. Jorum, B. Winner and A. Lampert (2019). "Pain relief in a neuropathy patient by lacosamide: Proof of principle of clinical translation from patient-specific iPS cell-derived nociceptors." EBioMedicine **39**: 401-408.
Nassar, M. A., M. D. Baker, A. Levato, R. Ingram, G. Mallucci, S. B. McMahon and J. N. Wood (2006). "Nerve injury induces robust allodynia and ectopic discharges in Nav1.3 null mutant mice." Mol Pain **2**: 33.
Osteen, J. D., K. Sampson, V. Iyer, D. Julius and F. Bosmans (2017). "Pharmacology of the Nav1.1 domain IV voltage sensor reveals coupling between inactivation gating processes." Proceedings of the National Academy of Sciences **114**(26): 6836-6841.
Power, K. E., K. P. Carlin and B. Fedirchuk (2012). "Modulation of voltage-gated sodium channels hyperpolarizes the voltage threshold for activation in spinal motoneurones." Exp Brain Res **217**(2): 311-322.
Renganathan, M., T. R. Cummins and S. G. Waxman (2001). "Contribution of Na(v)1.8 sodium channels to action potential electrogenesis in DRG neurons." J Neurophysiol **86**(2): 629-640.
Renganathan, M., S. Dib-Hajj and S. G. Waxman (2002). "Nav1.5 underlies the 'third TTX-R sodium current' in rat small DRG neurons." Molecular Brain Research **106**(1): 70-82.
Rogers, M., N. Zidar, D. Kikelj and R. W. Kirby (2016). "Characterization of Endogenous Sodium Channels in the ND7-23 Neuroblastoma Cell Line: Implications for Use as a Heterologous Ion Channel Expression System Suitable for Automated Patch Clamp Screening." Assay Drug Dev Technol **14**(2): 109-130.
Rühlmann, A. H., J. Körner, R. Hausmann, N. Bebrivenski, C. Neuhof, S. Detro-Dassen, P. Hautvast, C. A. Benasolo, J. Meents, J. P. Machtens, G. Schmalzing and A. Lampert (2020). "Uncoupling sodium channel dimers restores the phenotype of a pain-linked Na(v) 1.7 channel mutation." Br J Pharmacol **177**(19): 4481-4496.
Rush, A. M., T. R. Cummins and S. G. Waxman (2007). "Multiple sodium channels and their roles in electrogenesis within dorsal root ganglion neurons." J Physiol **579**(Pt 1): 1-14.
Rush, A. M., S. D. Dib-Hajj, S. Liu, T. R. Cummins, J. A. Black and S. G. Waxman (2006). "A single sodium channel mutation produces hyper- or hypoexcitability in different types of neurons." Proceedings of the National Academy of Sciences of the United States of America **103**(21): 8245-8250.
Sheets, M. F. and D. A. Hanck (1999). "Gating of skeletal and cardiac muscle sodium channels in mammalian cells." J Physiol **514 (Pt 2)**(Pt 2): 425-436.
Stiles, P. J. and C. G. Gray (2021). "Improved Hodgkin–Huxley type model for neural action potentials." European Biophysics Journal **50**(6): 819-828.
Tan, J. and D. M. Soderlund (2009). "Human and rat Nav1.3 voltage-gated sodium channels differ in inactivation properties and sensitivity to the pyrethroid insecticide tefluthrin." Neurotoxicology **30**(1): 81-89.
Tang, Z., Z. Chen, B. Tang and H. Jiang (2015). "Primary erythromelalgia: a review." Orphanet J Rare Dis **10**: 127.
Tavares-Ferreira, D., S. Shiers, P. R. Ray, A. Wangzhou, V. Jeevakumar, I. Sankaranarayanan, A. M. Cervantes, J. C. Reese, A. Chamessian, B. A. Copits, P. M. Dougherty, R. W. t. Gereau, M. D. Burton, G. Dussor and T. J. Price (2022). "Spatial transcriptomics of dorsal root ganglia identifies molecular signatures of human nociceptors." Sci Transl Med **14**(632): eabj8186.

Thompson, C. H., F. Potet, T. V. Abramova, J.-M. DeKeyser, N. F. Ghabra, C. G. Vanoye, J. J. Millichap and A. L. George, Jr (2023). "Epilepsy-associated SCN2A (NaV1.2) variants exhibit diverse and complex functional properties." Journal of General Physiology **155**(10).
Tigerholm, J., T. N. Hoberg, D. Brønnum, M. Vittinghus, K. S. Frahm and C. D. Mørch (2020). "Small and large cutaneous fibers display different excitability properties to slowly increasing ramp pulses." J Neurophysiol **124**(3): 883-894.
Tigerholm, J., M. E. Petersson, O. Obreja, E. Eberhardt, B. Namer, C. Weidner, A. Lampert, R. W. Carr, M. Schmelz and E. Fransén (2015). "C-fiber recovery cycle supernormality depends on ion concentration and ion channel permeability." Biophys J **108**(5): 1057-1071.
Tigerholm, J., M. E. Petersson, O. Obreja, A. Lampert, R. Carr, M. Schmelz and E. Fransén (2014). "Modeling activity-dependent changes of axonal spike conduction in primary afferent C-nociceptors." J Neurophysiol **111**(9): 1721-1735.
Tigerholm, J., A. H. Poulsen, O. K. Andersen and C. D. Mørch (2019). "From Perception Threshold to Ion Channels-A Computational Study." Biophys J **117**(2): 281-295.
Vacher, H., D. P. Mohapatra and J. S. Trimmer (2008). "Localization and targeting of voltage-dependent ion channels in mammalian central neurons." Physiol Rev **88**(4): 1407-1447.
Vasylyev, D. V., C. Han, P. Zhao, S. Dib-Hajj and S. G. Waxman (2014). "Dynamic-clamp analysis of wild-type human Nav1.7 and erythromelalgia mutant channel L858H." Journal of Neurophysiology **111**(7): 1429-1443.
Vasylyev, D. V. and S. G. Waxman (2012). "Membrane properties and electrogenesis in the distal axons of small dorsal root ganglion neurons in vitro." J Neurophysiol **108**(3): 729-740.
Verma, P., M. Eaton, A. Kienle, D. Flockerzi, Y. Yang and D. Ramkrishna (2020). "Examining Sodium and Potassium Channel Conductances Involved in Hyperexcitability of Chemotherapy-Induced Peripheral Neuropathy: A Mathematical and Cell Culture-Based Study." Front Comput Neurosci **14**: 564980.
Wang, D. W., K. Yazawa, A. L. George and P. B. Bennett (1996). "Characterization of human cardiac Na+ channel mutations in the congenital long QT syndrome." Proceedings of the National Academy of Sciences **93**(23): 13200-13205.
Wang, J., S. W. Ou and Y. J. Wang (2017). "Distribution and function of voltage-gated sodium channels in the nervous system." Channels (Austin) **11**(6): 534-554.
Wang, T., Y. Wang, J. Shen, L. Wang and L. Cao (2022). "Predicting Spike Features of Hodgkin-Huxley-Type Neurons With Simple Artificial Neural Network." Frontiers in Computational Neuroscience **15**.
Whitaker, W. R., J. J. Clare, A. J. Powell, Y. H. Chen, R. L. Faull and P. C. Emson (2000). "Distribution of voltage-gated sodium channel alpha-subunit and beta-subunit mRNAs in human hippocampal formation, cortex, and cerebellum." J Comp Neurol **422**(1): 123-139.
Yang, Y., Y. Wang, S. Li, Z. Xu, H. Li, L. Ma, J. Fan, D. Bu, B. Liu, Z. Fan, G. Wu, J. Jin, B. Ding, X. Zhu and Y. Shen (2004). "Mutations in SCN9A, encoding a sodium channel alpha subunit, in patients with primary erythermalgia." J Med Genet **41**(3): 171-174.
Yu, F. H. and W. A. Catterall (2003). "Overview of the voltage-gated sodium channel family." Genome Biol **4**(3): 207.
Zhang, X., B. T. Priest, I. Belfer and M. S. Gold (2017). "Voltage-gated Na(+) currents in human dorsal root ganglion neurons." Elife **6**.